Rotation of electrothermal-instability-driven overheating structure due to helically oriented surface magnetic field on a high-current-density aluminum rod

Awe, T. J.
Yu, Edmund
Shipley, Gabriel Alan
Yates, Kevin Colligan
Tomlinson, Kurt
Hatch, Maren W

To be published in: Physics of Plasmas

DOI to publisher's version: 10.1063/5.0279628

Rotation of electrothermal-instability-driven overheating structure due to helically-oriented surface magnetic field on a high-current-density aluminum rod

T. J. Awe,[1,a)] E. P. Yu[1], G.A. Shipley[2], K. C. Yates[1], K. Tomlinson[3], and M. W. Hatch[1]

[1] Sandia National Laboratories, Albuquerque, New Mexico 87185, USA
[2] Los Alamos National Laboratory, Los Alamos, New Mexico 87545, USA
[3] General Atomics, San Diego, California 92121, USA
[a)] Author to whom correspondence should be addressed: tjawe@sandia.gov

Abstract

Experiments on the 1-MA, 100-ns-risetime Mykonos Facility demonstrate rotation of electrothermal instability (ETI)-driven overheating structure on 1.00-mm-diameter, 10-nm-surface roughness, 99.999%-pure aluminum rods which are pulsed with helically-polarized surface magnetic field. Rods are machined to include pairs of 10-micron-scale quasi-hemispherical voids or "engineered defects (ED)" which provide the dominant current density perturbation from which ETI grows most rapidly. Experiments include an axial magnetic field component through the addition of a helically-wound return-current electrode or "helical return can (HRC)." For a given HRC design, azimuthal field (B_θ) and axial field (B_z) components rise at a prescribed and fixed ratio, driving an increasing magnetic field of constant polarization at the rod's surface; most experiments generated surface magnetic field at a 15-degree field polarization angle (from horizontal) defined as ϕ_B=arctan(B_z/B_θ). ETI-driven emission patterns from individual ED are observed to rotate along ϕ_B, while emission patterns from dielectric-coated ED pairs are shown to elongate and preferentially merge along ϕ_B, in qualitative agreement with 3D-magnetohydrodynamic simulations. These data strongly support that for a randomized distribution of current density perturbations on a high-current density conductor, nearby perturbations will favorably merge about ϕ_B, with the degree of merging increasing with current. Such observations offer fundamental new understanding of the seeding mechanisms of the helical magneto-Rayleigh Taylor (MRT) instabilities observed from axially-magnetized magnetically-driven imploding liners.

Section I: Introduction to helical instabilities on axially magnetized z pinches

Axial field in MagLIF fusion systems

Fast z pinches, in general, consist of an annular, axially-flowing, fast current pulse (e.g., ~100 ns risetime) which generates an azimuthal magnetic field, resulting in radial compression of the current-carrying material via the Lorentz Force. Z pinch configurations include single wires/rods, arrays of wires, gas puffs, and imploding liners (cylindrical thick-walled tubes or cylindrical thin-walled foils) and are broadly applicable to controlled thermonuclear fusion [i,ii,iii,iv,v,vi], the production of intense x-rays [vii,viii], and the study of laboratory astrophysics [ix]. Z pinches are physics-rich platforms, with open questions concerning their current carrying properties, material phase changes, implosion dynamics, stability, and stagnation properties.

This article applies most directly to the detailed current carrying properties of thick-walled imploding metallic liners, where the liner's wall thickness is much larger than the metal's room temperature magnetic field skin depth. Such liners can be used to both compress and inertially confine preheated and premagnetized fusion fuel in Magneto-Inertial Fusion (MIF) systems [x,xi,xii]. In Magnetized Liner Inertial Fusion (MagLIF [xiii,xiv,xv,xvi,xvii]), the preeminent MIF concept, an external Helmholtz coil pair premagnetizes the liner and the fusion fuel within to an axial field strength B_z=10-30 T [xviii]. The coils are driven with a several-millisecond risetime so that B_z is "static" in the sense that it is fully diffused and

uniform within the liner-fuel system before a ~20 MA, 100 ns current is pulsed on the liner's outer surface to drive the implosion. Fuel premagnetization is fundamental to the MagLIF concept, and experiments demonstrate enhanced stagnation performance (e.g., plasma temperature, neutron yield [xix,xx]), and magnetization of tritons [xxi,xxii] as a direct result of this applied and subsequently liner-compressed B_z.

Early MagLIF-relevant experiments demonstrate that inclusion of static B_z has transformative impact on the implosion dynamics of the metallic liner [xxiii,xxiv]. For liners imploded without axial premagnetization, largely azimuthally symmetric magneto-Rayleigh Taylor (MRT) instabilities develop [xxv,xxvi]. This is expected due to magnetic tension, since the fastest growing MRT modes align with a wave vector (**k**) that is perpendicular to the azimuthal drive field such that $k_z \bullet B_\theta = 0$ (note, however, that perfect alignment is not required for a mode to grow). By contrast, helically-oriented instability structures develop for liners premagnetized with static B_z~10 T. Initially, perhaps, this result seems intuitive, since, early in the experiment when the axial current is low, the magnetic field polarization angle at the liner's outer surface $\phi_B(t) \equiv \arctan[B_z(t)/B_\theta(t)]$ is large ($B_z \sim B_\theta$, thus $\mathbf{k} \bullet \mathbf{B} \sim 0$ for helically oriented perturbations). But significant ϕ_B is presumably short-lived because B_θ is expected to grow to >1000 T, whereas B_z is expected to remain nearly constant, at ~10 T. Therefore, since $\phi_B(t) \sim 0$ for all but the earliest (pre-implosion) stages of the experiment azimuthally symmetric MRT was expected. Data, however, show dominant and persistent helical instability modes. Furthermore, the pitch angle of the observed helices grow steeper as the liner implodes, suggesting that the helical modes are somehow "locked" to the liner's surface.

Axial magnetic field may have further utility to MagLIF by improving liner implosion stability through a dynamic screw pinch (DSP) mechanism. A DSP includes a helically-wound return-current path, or helical return can (HRC) which is coaxial with the liner and drives a time-varying axial magnetic field, $B_z(t)$, at the liner's surface. Here the axial field is "dynamic" in the sense that it is driven with the same rise time as the driver current, and, prior to liner implosion, the surface polarization angle ϕ_B will remain constant for a given HRC design. However, as the liner implodes, at the liner's surface $B_\theta(t) = \mu_0 I(t)/2\pi r(t)$ increases more rapidly than $B_z(t)$, since $B_\theta(t)$ increases as the liner radius, r(t), falls, thus driving ϕ_B downward (toward the horizontal). Time varying ϕ_B results in a continuous change in which MRT mode is most unstable as the liner implodes, resulting in a reduction in the accumulated growth time for any one mode. For MagLIF-like liners, theory suggests that linear MRT growth should be reduced by one to two orders of magnitude via the DSP method [xxvii]. Magnetohydrodynamic (MHD) simulations suggest [xxviii, xxix] that DSP-driven liners should evolve with a persistent helical instability, with a pitch angle that both grows for higher initial ϕ_B and increases as the liner implodes. Data from Z experiments suggest that the DSP improves liner-implosion stability, though detailed analysis has yet to be published.

Hypothesis concerning helical instability formation and evolution

Fundamental questions regarding instability development on axially magnetized imploding liners remain, including: (1) when is a helical perturbation initiated? And (2), under what conditions does the helical perturbation grow/persist throughout the implosion? When considering these questions, we distinguish 4 general field-polarization-evolution scenarios for thick-walled metallic liners:

In **Scenario 1 (static B_z, no flux compression)**, static field is provided by external Helmholtz coils, B_z is fully diffused and uniform prior to the liner implosion, and no axial flux compression occurs at the liner's outer surface. The field is initially purely axial (prior to Z's current delivery), followed by a brief pre-implosion stage, where $B_z \sim B_\theta$, followed by $B_\theta >> B_z$ for the remainder of the experiment. Here, helical modes are only reasonably seeded pre-implosion while $B_z \sim B_\theta$. Early helical seeds could grow due to electrothermal instability (ETI) driven liner-surface melt [xxx, xxxi, xxxii]. The time and orientation of melt may also be influenced by energy deposition from magnetically insulated transmission line (MITL) flow plasmas [xxxiii] where energetic particles bombarding the liner's surface may drive helically-oriented heating.

The remaining scenarios consider $B_z(t)$ which grows throughout the experiment. In **Scenario 2 (static B_z, compressed flux)** static axial field is generated from external coils as in Scenario 1, but now MITL-generated low-density plasmas with sufficient electrical conductivity to advect magnetic field enter the target region and implode via the Lorentz Force to compress B_z to near 1000 T [xxxiv,xxxv], supporting persistent $\phi_B(t)$ and enabling the possibility of helical mode seeding throughout the experiment. In **Scenario 3 (Hall instability)** static field is generated as in Scenario 1, but now an interchange instability within a low-density coronal plasma (e.g., 10^{15} cm^{-3}) generates helical plasma filaments on the liner's outer surface which carry helical current [xxxvi,xxxvii,xxxviii]. This current aligns with the magnetic field and is thus force free. The force-free configuration persists to generate increasing $B_z(t)$ throughout the experiment, supporting persistent $\phi_B(t)$. In **Scenario 4 (DSP)**, there is no static applied field, but rather $B_z(t)$ increases linearly with current, conceivably to 100s of T, via the DSP mechanism [xxvii, xxviii]. Qualitatively then, **Scenarios 2-4** all include helically polarized surface magnetic field at the liner's surface throughout (albeit by distinct mechanisms) making the persistence of helical modes expected relative to **Scenario 1**.

Helical instability development has been considered theoretically and computationally. For example, relevant to **Scenario 1 (static B_z, no flux compression)**, Weis *et al*., used ideal MHD and linear perturbation theory to evaluate the coupling of sausage and kink modes to MRT for the cases of thin and thick imploding liners with uniform B_z inside, within, and outside of the current carrying metal [xxxix]. Instabilities of the form $\exp(im\Theta - i2\pi z/\lambda)$ develop, where m is the azimuthal mode number, and λ is the perturbation wavelength. In the absence of B_z, m=0 sausage modes dominate, while higher-order modes (m>0) grow more rapidly when B_z is present. Larger B_z "unlock" higher mode numbers, enabling growth of multiple intertwined helices, in qualitative agreement with the structures observed in [xxiii]. Furthermore, when B_z is present, m=0 mode growth is delayed, and the growth rate is reduced versus higher mode numbers, potentially explaining the persistence of helical modes in **Scenario 1**, even if $B_\theta >> B_z$ for much of the experiment. Also, 3D MHD simulations [xxiv] showed that if helical surface perturbations can be seeded pre-implosion the perturbation will grow, even in the absence of applied helical field.

Other studies have focused on helical instability evolution for $B_z(t) \sim B_\theta(t)$, i.e., for **Scenarios 2-4**. For example, relevant to **Scenario 2 (static B_z, compressed flux)** Seyler *et al*., have shown computationally using the extended MHD (XMHD) code PERSEUS [xxxv] that such a flux-compression mechanism can result in strong $B_z(t)$ at the liner's surface to support helical instability growth. Later, to explore **Scenario 3 (Hall instability)**, PERSEUS was again used to model the impact of Hall physics on helical-mode generation, but now the low-density plasma is localized to a coronal plasma layer which surrounds the liner [xxxvii]. For simulations initialized with an ad-hoc low-density plasma layer, helical modes grow and persist both for foils driven at 1 MA current, or MagLIF-like liners driven by 20-60 MA current. Finally, relevant to **Scenario 4 (DSP)**, Shipley *et al*. have presented 3D MHD simulations which demonstrate that helical modes grow from liners seeded with a random/white-noise perturbation when driven by the DSP mechanism [xxix]. Axial flux compression is not required for helical-instability growth for the DSP mechanism, but the possibility of MITL-generated plasmas driving flux compression exists.

Helical instability experimental studies at 1 MA

Various 1-MA-scale experiments have explored helical instability growth from z pinches with applied B_z. Given the reduced peak current versus Z, not all pertinent imploding-liner physics can be evaluated in a single experiment. For example, implosion physics can only be studied using thin-foil liners (e.g., 100's of nm wall thickness). For a ~100 ns current pulse such foils are much thinner than the current-carrying skin depth, causing the foil to explode and increase in thickness by a factor of 100 or more. Such exploding-foil physics is absent in Z liners, which have wall thickness of 100s of μm, allowing current to initially flow

in a surface skin layer and gradually diffuse inward. Therefore, if the experimenter chooses to study helical-instability initiation pertinent to "thick" metal, the z pinch is too massive to be imploded by a 1 MA current, and acceleration-driven MRT cannot be studied. Despite such limitations, a variety of key observations have been made on 1-MA-class drivers over the last decade, which are summarized next.

Experiments by Atoyan *et al*. [xl], evaluated non-imploding thin-foil liners for both dynamic (HRC-generated) and static (Helmholtz-coil-generated) B_z. For both types of B_z, extreme ultraviolet (XUV) emissions from foil surfaces were helical, and the handedness of the helical emissions flipped according to the orientation of the axial field. Images were gathered after peak current; thus, data cannot inform the physics of the seeding mechanism, and given the absence of implosion, results aren't applicable to MRT. Next, Yager-Elorriaga *et al*., produced a series of relevant papers [xli, xlii, xliii], discussing instability development in the presence of static B_z for non-imploding, imploding, and exploding metallic-foil liners. For non-imploding liners, foils were placed directly over an insulating cylindrical support which was either flat/unseeded or helically seeded. For unseeded supports, m=0 modes grew in the absence of B_z, whereas helical modes grew when a 1-2 T static B_z was applied. For helically-seeded liners, application of a 1-2 T static B_z was shown to reduce instability development when the handedness of the field was opposite that of the seed perturbation. Complementary experiments allowed the foil to implode. The imploding plasma eventually stagnated upon a central dielectric support rod, and later expanded. Data show helical modes develop when B_z is applied, and the pitch angle of the helix increases as the liner implodes and then decreases after the liner stagnates on the support and rebounds radially outward, suggesting robust helical mode locking. Data are shown to be largely consistent with mode locking in thick liners, including the experimental observations in [xxiii] and in the analytic theory of Weis [xxxix], but neither of these thick-liner studies considered instability evolution after rebound. Finally, DSP physics was studied by Campbell et al [xliv, xlv]. Here, thin metallic foils imploded by the DSP mechanism developed helical modes. Versus standard (B_z=0) pinches, MRT amplitudes were reduced for DSP-driven liners, with reduced growth as the field polarization angle ϕ_B was increased.

All aforementioned studies from 1-MA-class drivers focused on thin-foil liners, with results reported on the evolution of well-established instabilities and no direct observations of the initialization of the helical seed perturbation. By contrast, the experiments reported in this paper were designed to study the initiation of an ETI-driven helical seed perturbation on the surface of thick aluminum rods.

The work reported in this manuscript is an extension of previous thick-rod experiments [xlvi,xlvii ,xlviii, xlix, l, li, lii, liii, liv, lv] and in particular "engineered defect (ED)" platform results [lvi]. ED-z-pinch targets are machined from 99.999% pure aluminum or "Al 5N" to a 1.00-mm-central rod diameter with ~10-nm-surface roughness. The 1.00-mm-diameter surface is then further machined to include pairs of 10-micron-scale quasi-hemispherical voids (i.e., EDs), which are the dominant current-density perturbation in the rod's surface. EDs emulate native defects (i.e., micron-scale voids and resistive inclusions) that commonly occur in metals, while ultrapure (i.e., defect-free), ultrasmooth aluminum provides a clean background for studying current-driven ETI evolution. Paired EDs provide insight into how isolated defects merge to form larger structures. The well-defined initial conditions in previous experiments enabled detailed comparison of data on ED-seeded ETI evolution with 3D MHD simulation [lvii, lviii, lix]. Like these previous experiments, rods were pulsed to nearly 1 MA in 100 ns, but now the magnetic field at the rod surface was modified to include an axial component, $B_z(t)$, through the addition of an HRC.

The remainder of the manuscript is organized in the following way. In Section II ETI theory is presented and analytic solutions for current density enhancement near simple perturbations are provided. In Section III detailed 3D-MHD simulations are presented, with results from simulations driven both with purely azimuthal (B_z=0) and dynamically-applied helical magnetic field. Together, theory and simulation

predict experimental observables which then inform the experimental objectives and expectations detailed in Section IV. In Section V, we specify the experimental setup, including details of a new ED target, and the design of an HRC which can drive a ϕ_B=15° surface field polarization on a 1.0-mm-diameter rod. Next, in Section VI, we discuss experimental results. Our analysis focuses on visible-spectrum self-emission images (2 ns/3 μm temporal/spatial resolution) about surface ED. First, we discuss results from bare rods and focus on rotation of the early heating from individual ED. Next, we discuss results from dielectric coated rods, and focus on the heating and merging process for closely-paired ED. In Section VII, concluding remarks are made. Finally, several appendices are included: Appendix 1 details ALEGRA simulations, Appendix 2 details hardware commissioning challenges, Appendix 3 discusses a potential ED machining asymmetry that may impact experimental emission profiles, and Appendix 4 provides a detailed description of dielectric-coating fabrication.

Section II: Introduction to the electrothermal instability (ETI) and engineered defects (EDs)

Any inhomogeneity in an intensely Joule heated conductor will alter current density, resulting in nonuniform heating and expansion due to the electrothermal instability (ETI). ETI is a Joule-heating-driven instability which occurs due to the change in electrical resistivity (η) with temperature (T). For example, a resistive obstruction will divert current density (j), leading to locations of enhanced j and Joule heating (ηj^2), increasing T. For condensed solid and liquid metal ($\partial\eta/\partial T > 0$), these locations become more resistive, thus growing the spatial extent of the resistive obstruction. Upon transition to vapor and plasma, resistivity tends to fall with temperature ($\partial\eta/\partial T < 0$), again diverting current and generating local overheating structures of a different orientation. It can be shown through linear theory under MHD approximations [lx, xxxii, lix] that for a perturbed, thin, current-carrying slab, the fastest growing ETI modes tend to align perpendicular to the current as "ETI strata" for condensed metal, and parallel to the current flow as "ETI filaments" in the plasma state. Assuming perturbations of the form $e^{\gamma t+ikz}$ (z is the direction of current flow) and neglecting hydrodynamic motion, Ref. [xxx] derives the striation growth rate $\gamma = \frac{\frac{\partial \eta}{\partial T} j^2 - k^2 \kappa}{\rho c_V}$, where κ, ρ, c_V are the thermal conductivity, mass density, and specific heat, respectively. For magnetically-driven-liner applications (with B_z=0), the striation form of ETI is most concerning since it is ideally oriented to seed subsequent MRT growth. Indeed, 2D MHD simulations [lxi] show that ETI growth on imploding liners can provide the primary seed for subsequent MRT growth. These results have been supported by data from liner-implosion-dynamics studies on Z [lxii, lxiii].

It is important to understand how the numerous and randomly distributed voids and resistive inclusions within a metal heat in isolation, and furthermore, if and how they align/merge to form larger perturbations. Towards that goal, flow around an individual isolated perturbation can be understood using the analogy between hydrodynamic and electrical current flow [lvii, lxiv]. In the case of a spherical void of radius R embedded in a uniform current density $\boldsymbol{j} = j_0\hat{z}$. (Fig. 1(a)), the solution for **j** outside the sphere can be expressed as the gradient of a potential φ: $\boldsymbol{j} = -\nabla\varphi$, where $\varphi = -j_0 z\left(1+\frac{R^3}{2\xi^3}\right)$. In spherical coordinates, we obtain $j_\xi = j_0\cos\alpha\left(1-\frac{R^3}{\xi^3}\right)$, $j_\alpha = -j_0\sin\alpha\left(1+\frac{R^3}{2\xi^3}\right)$, where ξ and α represent radial distance and polar angle, respectively. Along a lineout $\mathcal{L}$ passing through the center of the sphere and lying along the equatorial plane $\alpha=\pi/2$ (see Fig. 1(a)), the solution can be expressed in Cartesian coordinates: $\boldsymbol{j} = j_0\left(1+\frac{R^3}{2|x|^3}\right)\hat{z}$. This solution, plotted in Fig. 1(b), shows that j is enhanced by 3/2 at x=R and falls as x increases. As seen in Fig. 1(a), j also falls along the surface of the sphere when approaching the poles, with j=0 at top and bottom "stagnation points." Joule heating is thus maximized about the equator, increasing the resistivity locally (for $\partial\eta/\partial T>0$) and extending the influence of the resistive perturbation about the equatorial plane. Note that the analytic solution is found by considering

a sphere embedded in a uniform metal of infinite extent, but the solution is also applicable to the scenario of hemispherical ED cut into the surface of an infinite half-space, since the solution is symmetric about a plane through the center of the sphere.

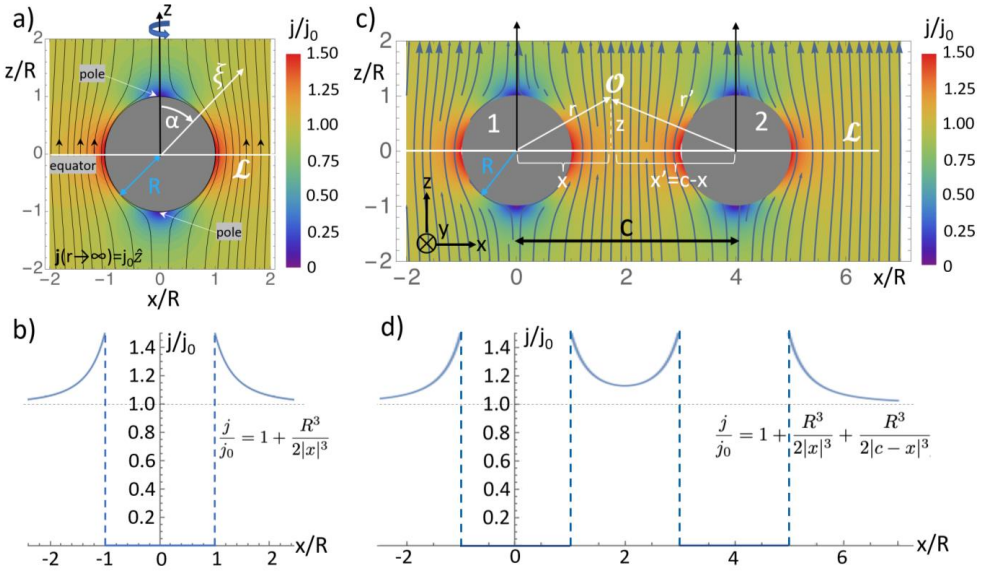

Figure 1: (a) Flow around a spherical void of radius R immersed in a uniform flow j_0. Color denotes j/j_0 while black lines are **j** streamlines. The visualization plane cuts through the center of the sphere; the full 3D solution is obtained by rotating the pattern about the z axis. (b) Solution for j/j_0 along the lineout $\mathcal{L}$ in (a). (c) Pair of spherical voids, separated by distance c, immersed in uniform flow j_0. The visualization plane cuts through the center of both voids at y=0 (the y-coordinate points into the page) and r, r′ denote the distance to the observation point $\mathcal{O}$. Unlike the single sphere solution in (a), the solution in (c) does NOT possess rotational symmetry about the z-axis. (d) solution for j/j_0 along lineout $\mathcal{L}$ in (c).

This model can be extended to estimate the current density amplification for a pair of spheres of radius R, separated by distance c, again immersed in uniform current density j_0 (Fig. 1(c)). In the limit $R/c \ll 1$, an approximate solution exists in the hydrodynamic case (see for instance [lxv], Sect. 17.40), from which we can infer the electrical solution $\varphi \cong -j_0 z\left(1+\frac{R^3}{2r^3}+\frac{R^3}{2r'^3}\right)$, where $r=\sqrt{x^2+y^2+z^2}$ and $r'=\sqrt{(c-x)^2+y^2+z^2}$ represent the distance to the observation point $\mathcal{O}$ from the left and right spheres, respectively. The 3 terms in the potential φ represent, in order, the free-stream current $j_0\hat{z}$, the correction to **j** due to the left sphere, and correction due to the right sphere. The current density $j=|\boldsymbol{j}|=|\nabla\varphi|$ is plotted in Fig. 1(c) in the y=0 plane. Along the lineout $\mathcal{L}$ connecting the spheres in the equatorial plane (z=0, y=0), the solution is: $\boldsymbol{j}=j_0\left(1+\frac{R^3}{2|x|^3}+\frac{R^3}{2|c-x|^3}\right)\hat{z}$, which is plotted in Fig. 1(d). As expected from the single sphere solution, j peaks at the sides of each sphere individually, while also amplifying between the spheres due to the superposition of their deflected flows. For instance, between the spheres, at x=c/2, $j=j_0\left(1+\frac{(2R)^3}{c^3}\right)$, so for 2R/c=1/3 (as is the case in the experiments, see Section V-c, Fig. 10), the amplification above the free streaming value is quite small—$j=j_0\left(1+\frac{1}{27}\right)$—but is nevertheless sufficient to provide a seed for ETI-driven merging between spheres.

Section III: ED simulations

The analytic models described in Sect. II are useful for understanding the initial redistribution of **j** around EDs at early time when the surrounding metal has spatially constant electrical conductivity $\sigma=1/\eta$. However, once localized Joule heating causes significant temperature increase so that σ is spatially varying, the analytic models no longer hold. To understand further ED evolution, we must turn to numerical simulation. All reported aluminum-rod simulation results are from the MHD code ALEGRA [lxvi, lxvii], which uses a SESAME equation of state [lxviii], including material strength (elastic-plastic constitutive model [lxix] combined with Steinberg-Guinan-Lund yield model [lxx]). Electrical and thermal conductivities are provided by the Lee-More-Desjarlais model [lxxi]. Simulations assume ion and electron temperatures are equal and do not account for radiative losses. Further simulation details may be found in Appendix 1.

Simulations consider a 1-mm-diameter aluminum rod driven by ~0.85-MA, ~100-ns-risetime current pulse (see Fig. 2(h)) which is roughly comparable to the Mykonos current (see Fig. 8(d)). Similar to experimental targets, EDs are quasi-hemispheres with rim diameter D_{rim}=24 μm and 6 μm depth (see Fig. 6 of [lvi], and Fig. 10 of this manuscript). First, we discuss ETI evolution from an ED in bare aluminum rods for both B_z=0 and dynamic $B_z(t)>0$ (i.e., rods driven by a HRC with ϕ_B=15°). We report simulation results from single ED rather than from ED pairs, since for bare rods, surface plasma generally forms before extensive pair merging occurs. Next, we discuss ETI evolution from dielectric-coated ED, again for both B_z=0 and for ϕ_B=15°. Here, we report results both from single ED and for ED pairs, since for dielectric-coated rods surface plasma formation is delayed by 10s of ns [l] allowing the observation of ED-pair merging in experiments.

Section III-a: ETI evolution from ED in bare (uncoated) rods

Bare ED, B_z=0

The evolution of bare EDs in current-driven metal has been described in detail in Refs [lvi, lviii, lix]. To keep this manuscript self-contained, we provide the following synopsis: as shown in Fig. 2(a), **j** diverts around the ED and amplifies around its equator, driving enhanced Joule heating there. The resulting pressure gradient, seen in Fig. 2(b), causes melted metal to flow along $-\nabla p$ and focus azimuthally towards the ED center, forming a bump with similar electrical conductivity σ to the surrounding metal. Now, **j** is drawn into the bump (rather than away from the ED – contrast the **j** flow patterns in Figs. 2(a) and 2(c)), amplifying at the poles of the bump [lix, lxv], resulting in enhanced Joule heating there, as seen in Fig. 2(c). Consequently, peak Joule heating has shifted from the ED equator to the poles, which drives higher temperature at the polar "hot spots" (Fig. 2(e)), leading to enhanced emissions indicated by the synthetic visible emission (Fig. 2(g)) generated from the post-processing code SPECT3D [lxxii]. The brightly emitting spots at the pole locations are referred to in this manuscript as "polar emission" (note it was previously referred to as "cat eye" emission in [lvi]). As illustrated in Fig. 2(f), the hot spots responsible for polar emission eventually explode radially outward, resulting in lower-density-plasma plumes that develop ETI filaments directed along the direction of current flow (i.e. along z), which eventually dominate emissions (see Figs. 3(e,f) of [xlix] and Fig. 6 of [lviii]).

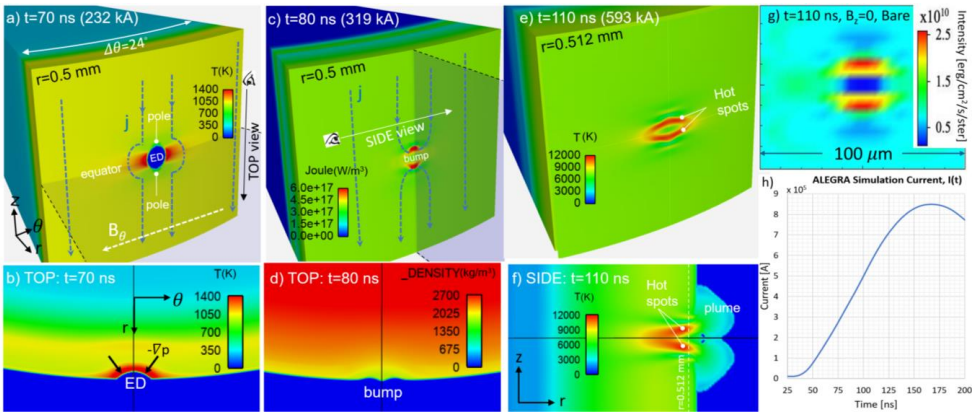

Figure 2: 3D ALEGRA simulation of a bare/uncoated engineered defect (ED) for the case B_z=0. The computational wedge is periodic in axial (z) and azimuthal (θ) directions. (a) Early temperature (T) of the rod surface (r=0.5 mm). Blue lines represent current density (**j**) streamlines, diverting around the ED and amplifying around its equator. Dashed black lines bound a fixed-z plane used to visualize the top view. b) Top view of ED, showing enhanced T around the ED equator and an azimuthally focusing pressure gradient. c) Joule heating on rod surface. Enhanced expansion at the ED equator generates a bump – see top view in (d). (e) Hot spot formation from poles due to enhanced Joule heating. Hot spots explode outward, as seen in the side view in f), which cuts through the ED center at a fixed-θ plane. (g) Synthetic visible emission image from SPECT3D, which solves the radiative transfer equation along lines-of-sight through the ALEGRA computational grid. At each volume element along the line-of-sight, the frequency-dependent absorption and emissivity of aluminum are computed under the assumption of local thermodynamic equilibrium (LTE). The resolution in the synthetic images is 4 μm (similar to experimental imagers) and the range of photon energies is 1.3-4.6 eV. (h) Current profile used in ALEGRA simulations.

Bare ED, B_z>0

In the presence of dynamic $B_z(t)$ generated by a helical return can (HRC), from $\nabla\times E=-\partial B/\partial t$, azimuthal j_θ will be generated on the rod's surface via eddy current induction, shielding the interior of the metal from the externally pulsed $B_z(t)$. This will result in helical current flow on the rod's surface. In the limit where the current skin depth δ is much smaller than rod radius, the current density vector **j** is approximately perpendicular to the magnetic field vector **B**. For an ED placed on the surface of the rod, the general evolution is predicted to be identical to that for B_z=0, but now, with the helical (rather than axial) **j**, the heating pattern will rotate. This scenario is illustrated in Fig. 3, which is identical to the bare ED shown in Fig. 2, but now with an external $B_z(t)=0.268B_\theta(t)$, or ϕ_B =15° applied at the rod's surface. In Figs. 3(a,b), **j**, **B**, T, and the polar emission pattern all rotate by ϕ_B relative to the B_z=0 case in Fig. 2.

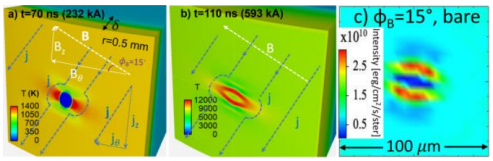

Figure 3: Bare ED in presence of dynamically applied $B_z(t)$. (a) Azimuthal j_θ is generated on the rod's surface via eddy current induction. Far from the ED, **j** is helical. Close to the ED, the **j** pattern is identical to the B_z=0 case in Fig. 2(a) but rotated by ϕ_B. (b) Rotated polar temperature topography at 110 ns, with (c) associated synthetic emission image.

Section III-b: ETI evolution from dielectric-coated ED

Dielectric-coated ED, B_z=0

Liners have shown improved implosion stability when coated with 10s of microns of dielectric, due to the dielectric's tamping of ETI-driven surface expansion, which reduces the seed for subsequent MRT growth [lxiii, lxxiii]. When studying ED evolution, dielectric coatings have an added benefit of delaying surface plasma formation, thus enabling extended study of strata formation and evolution in condensed metal. As a result, simulations have examined coated ED both in isolation, and configured in closely-spaced pairs. Fig. 4 shows a simulation of an isolated ED which has been filled and coated with a 40-μm thick layer of dielectric (Lexan). Recall from Figs. 2(c,d) that by t=80 ns, the bare ED has transformed into a bump, qualitatively altering **j** and resulting in the polar emission seen in Fig. 2(g). By contrast, Figs. 4(a,b) show that the coated/tamped ED remains a pit. This prevents development of the polar overheating pattern, seen from bare-ED in Fig. 2(c), so that by t=110 ns, the heating pattern for the coated ED is qualitatively different (see Fig. 4(c)).

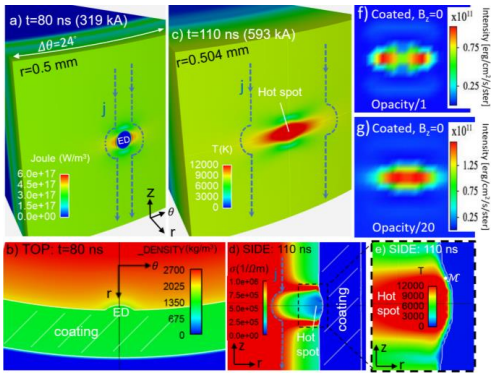

Figure 4: Dielectric-coated ED, B_z=0. (a) Joule heating on the surface of an aluminum rod at t=80 ns. Due to the tamping layer, heating peaks at the ED equator, rather than at the poles, as in Fig. 2(c). (b) Top view of coated ED. A bump has not formed. (c) Hot spot formation from a coated ED. "Polar emission" does not occur. (d) Side view of electrical conductivity shows that the coating tamps hot spot explosion and plume formation. **j** streamlines (in blue) divert around the hot spot, and polar emission never develops. (e) Magnified side view of the hot spot. $\mathcal{M}$ represents a mixed Al-dielectric cell with high opacity, which prevents bright emissions from the hot spot from being visible. Simulated visible emission images at t=110 ns post processed in SPECT3D with unmodified opacity in (f). In (g) the opacity has been reduced by a factor of 20, which increases the photon mean free path, allowing photons born from the hot spot to transport through mixed cells, resulting in bright emission from the hot spot location.

As seen in the side view in Fig. 4(d), thermal pressure in the hot spot has grown sufficient to transform the pit into a bump, despite the presence of the coating. In the bare case shown in Figs. 2(c,d), the bump consists of relatively cool (3300 K) and dense (1900 kg/m^3~0.7ρ_{solid}) melted metal with electrical conductivity σ similar to surrounding metal. Consequently, the hydrodynamic analogy with electrical current flow remains applicable, and **j** is pulled into the bump, leading to polar emission. In the coated case, the bump does not form until later, when it has reached temperature (~14,000 K) and density (~500 kg/m^3) such that σ in the bump is significantly lower than surrounding rod material, as seen in Fig. 4(d). Hence, **j** flows around the bump rather than into it, and polar emission does not develop.

Figure 4(e) shows a magnified view of the hot spot, highlighting details within the dashed black box of Fig. 4(d). At the interface between Al and the dielectric coating are mixed Al-dielectric cells with temperature intermediate between hot Al and cold dielectric. According to the opacity tables used, the density (~700 kg/m^3) and temperatures (~8000 K) correspond to high Al opacities (photon mean free path~30 nm at 3

eV energy). Hence, emission at these locations is dominated by the relatively cool mixed cells, resulting in dim emission at the hot spot location, as seen in Fig. 4(f). Because of uncertainties in the numerical accuracy of mixed cells, as well as the high opacity values themselves, we also ran SPECT3D with 20 times lower opacity, increasing the photon mean free path to 0.6 μm (slightly larger than resolution cell size). In this case, photons born from the hot spot can transport through the mixed cells, resulting in bright emission at the hot spot location (see Fig. 4(g)), which agrees better with experiment (see [Iv] and Section VI-b of this manuscript).

ETI strata formation between azimuthally-separated ED pairs for B_z=0 has also been simulated. Fig. 5 shows that **j** redistributes around each ED, adding constructively between them to drive local overheating and eventually ED-pair merging. Early in time at t=80 ns, EDs behave nearly independently; the single ED pattern (see Fig. 2(a)) is repeated about each ED, with T and Joule heating peaked at the ED equators. However, as described in Sect. II, superposition of diverted **j** leads to a slight increase in **j**, Joule heating (Fig. 5(c)), and T (Fig. 5(a)) between EDs. In addition, peak T at the sides of the EDs corresponds to a local reduction in σ, causing the low-σ ED region to widen, increasing ED-pair interaction.

By t=110 ns, redistribution of **j** between the EDs, combined with lower local σ, results in peak Joule heating occurring between EDs (Fig. 5(f)), in turn driving a merged temperature strip (Fig. 5(d)), which we can identify as an ETI striation. At this point, **j** preferentially flows along the lower resistance "outer" paths around the striation, rather than the low-σ "inner" paths (Fig. 5(e)) between EDs. Nevertheless, Joule heating between EDs remains elevated due to low σ. The striation should be experimentally diagnosable, as indicated by the synthetic emission image (Fig. 5(g)).

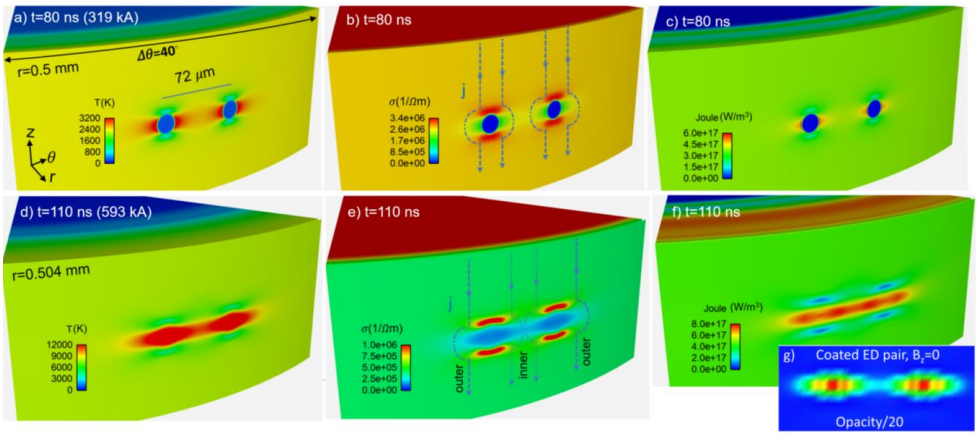

Figure 5: ED pair separated by 72 μm and coated with 35 μm of dielectric (not shown). (a), (b), and (c) Temperature, electrical conductivity, and Joule heating, respectively, on the surface of an aluminum rod at t=80 ns. Blue lines illustrate streamlines for current density **j**. (d), (e), and (f) Same quantities plotted at t=110 ns. EDs have merged due to enhanced Joule heating between EDs. Thinner **j** lines between EDs illustrate that **j** redistribution between EDs is weaker due to low σ there; **j** prefers to flow around the merged low-σ striation. (g) displays a synthetic self-emission image of the coated ED pair at 110 ns.

Dielectric-coated ED, B_z>0

As discussed for bare ED, in the presence of HRC-generated dynamic $B_z(t)$, azimuthal j_θ will be generated on the coated rod's metal surface via eddy current induction, resulting in helical current flow. **j**, **B**, and T will all rotate by ϕ_B relative to the B_z=0 case, and as a result, the emission patterns predicted in the synthetic emission image also rotate by ϕ_B. Fig. 6 shows simulation results from a coated ED pair, separated by 72 μm along a pair angle ϕ_{ED} =15°, which is parallel to the dynamically applied ϕ_B =15°. As shown, the heating and emission patterns about ED rotate by ϕ_B to align with the helical **B**. In the case of closely spaced ED pairs, we expect EDs to be more likely to merge when they are aligned to ϕ_B, rather than horizontally, as in the B_z=0 case.

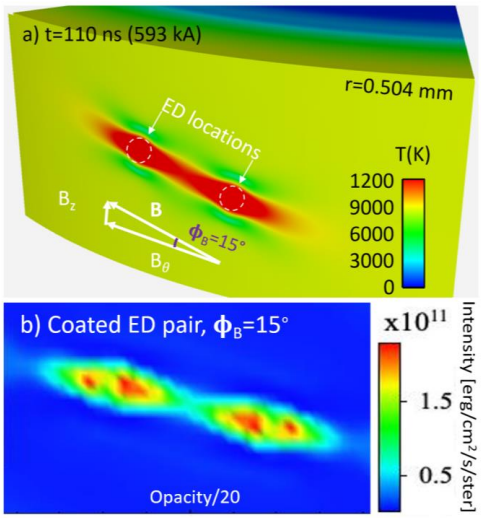

Figure 6: Coated ED pair in the case of dynamically applied $B_z(t)$. The pair is separated by 72 μm an oriented at a pair angle ϕ_{ED}=15° which is parallel to ϕ_B=15°. a) Temperature near the surface of the rod. b) Simulated visible emission from the ED pair.

Section IV: Experimental objectives and expectations

Here, we report results from experiments on the 1 MA, 100 ns risetime Mykonos Facility [lxxiv, lxxv], which extend the ED platform to study ETI evolution for dynamically-rising $B_z(t)$, generated by an HRC. Our experimental objective is to determine whether the expected changes in the self-emission patterns from ED targets due to ETI-driven heating occur. The schematic below shows at a high level the types of targets, the expected observables, and the nomenclature that will be used throughout this manuscript. First, the top row of Fig. 7 shows polar emissions (yellow) from isolated ED in two instances. In Fig. 7(a), ϕ_B=0° and the expected orientation of the polar emission is vertical (Θ_{pole}=0°). In Fig. 7(b), a helical magnetic field has been applied by an HRC resulting in a field polarization ϕ_B=15°; here, the expected polar emission angle is Θ_{pole}=15°. Note that we have defined positive values of both ϕ_B and Θ_{pole} for clockwise rotation. Next, in the second row, we indicate anticipated preferential pair merging (overheating emissions due to ETI strata formation, yellow) for dielectric-coated ED pairs which are well aligned to ϕ_B. Here, ED pair angles (ϕ_{ED}) are defined versus horizontal, where again, clockwise rotation is assigned as positive.

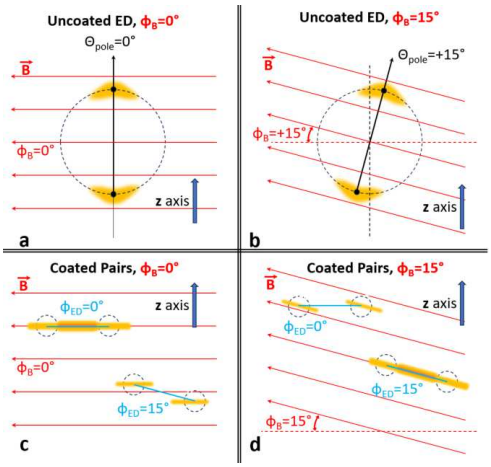

Figure 7. Schematic of expected observables and experimental nomenclature. Figs. (a) and (b) show expected polar emission from uncoated individual ED for cases of ϕ_B=0° and ϕ_B=15°, respectively. Figs. (c) and (d) show expected enhanced merging along ϕ_B for coated ED pairs for cases of ϕ_B=0° and ϕ_B=15°, respectively.

Section V: Experimental design and commissioning

Section V-a: Powerflow hardware design

A variety of recent studies [lvi, lv] on the Mykonos Facility have used powerflow hardware similar to the design shown in Fig. 8(a), which includes a cylindrical coaxial feed to deliver current to the z pinch target. When adding $B_z(t)$, to preserve peak current, the HRC cannot be too inductive, and so must be much smaller radius than the original SRC, which is accommodated by a newly designed "swooping" MITL (Fig. 8(b)) with an AK gap that falls from 9.0 mm to 3.4 mm to limit inductance. A new small-radius and low-inductance SRC (Fig. 8(c)) couples to the same swooping MITL. Mykonos machine current data, I(t), from the swooping feed are shown in Fig. 8(d), where the 12 red curves are for shots using a ϕ_B=15° HRC while the 11 black curves are for shots using an SRC. Data indicate minimally shorter rise time for the lower inductance SRC. Peak currents vary by nearly 100 kA over this dataset.

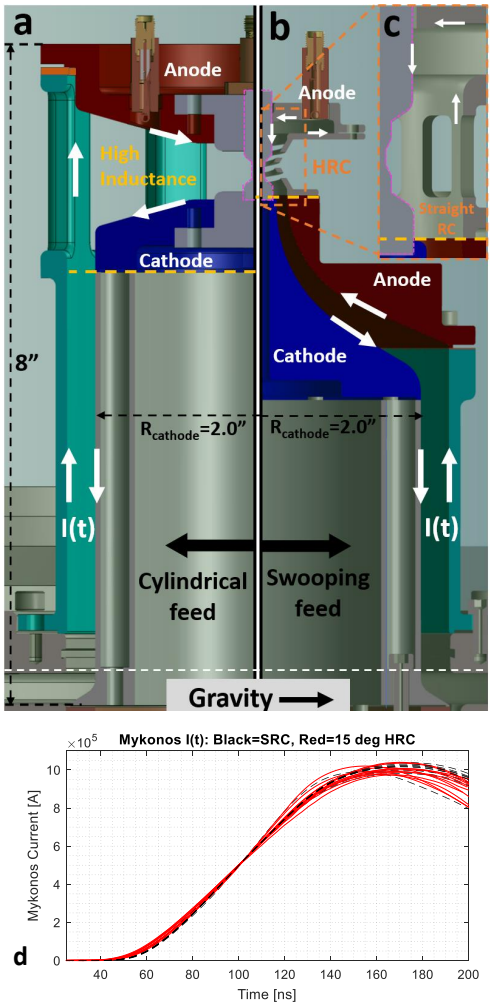

Figure 8. Mykonos powerflow hardware. (a) Cylindrical feed used in earlier ETI studies. (b) New, "swooping" current feed developed to transition to a small radius HRC (b) or small radius SRC (c). The direction of current flow is indicated by white arrows and the physics target is outlined in dashed-pink lines. A more detailed view of the target region is provided in Fig. 9. (d) Mykonos machine-current curves for experiments using the swooping feed and either a ϕ_B=15° HRC (Red) or SRC (dashed black).

The powerflow geometries of Fig. 8 differ in terms of the strength and location of maximum electric field, which could impact the generation of low-density plasmas. Explosive electron emission can be sourced from powerflow surfaces with an electric field strength E ≥ 240 kV/cm [lxxvi]. The field strength across the AK gap is calculated as $E=L_{downstream}*(dI/dt)/G$, where $L_{downstream}$ is the inductance of all downstream hardware, including the target region, and G is the local AK gap. For the hardware in Fig 8(a), the cylindrical feed gap is constant at G=0.90 cm, so the highest field strength occurs at the white dashed line where $L_{downstream}$=23 nH is largest. Here, for $(dI/dt)_{max}$~10 kA/ns (see Fig. 8(d)), the field strength is E=255

kV/cm. The explosive electron emission limit is therefore marginally exceeded, and only for powerflow surfaces far from the target. For the swooping feed driving the ϕ_B=15° HRC (Fig. 8(b)), by design intent, the inductance downstream of the white line is again 23 nH, so we expect similar marginal potential for explosive electron emission there. But, for this hardware, G falls in the swooping feed, reaching 3.4 mm at the end (yellow dashed line), where we estimate $L_{downstream}$=14.4 nH, suggesting the field may reach 422 kV/cm for dI/dt=10 kA/ns. Therefore, the explosive electron emission limit is exceeded at the entrance to the target region. Finally, for the hardware configuration in Fig. 8(c), the inductance downstream of the white dashed line is estimated to be 16 nH (177 kV/cm), with the target region inductance (that downstream of the yellow dashed line) estimated at only 6.7 nH (196 kV/cm). Therefore, explosive electron emission in not expected.

To evaluate the impact on target heating due to the possible influx of flow plasmas from the powerflow feed, experiments were conducted using the swooping feed and SRC of Fig. 8(c), but with an 8-nH-higher inductive cavity added downstream of the target. Therefore, in these experiments, the target region inductance is ~14.7 nH, or nearly identical to that of the HRC experiments. The additional inductance had no observable qualitative effect on the 3D topography of target-surface self-emission (i.e., ETI driven emissions from local defects were similar), suggesting that flow plasmas sourced from the feed, if indeed present, do not meaningfully impact target surface heating, ETI evolution, and self-emission.

Section V-b: HRC design

HRCs (Fig. 8(b) and Fig. 9(a,b)) were machined from 304 stainless steel and were designed to meet a variety of experimental requirements. (1) The HRC must allow diagnostic imagers to view the full 1.00-mm-diameter physics region of interest of the target (indicated by red in Fig. 9(a)) at two azimuthal locations separated by 180°. (2) It must provide $\phi_B(t)$=15° field polarization at the target's 1.00-mm-diameter surface. (3) The strength of the axial field about the central 1-mm height of the physics target must not vary by more than 10% to provide uniform ϕ_B. (4) The HRC geometry should prevent both shorting between the HRC and target as well as interhelix shorting through the time of peak current. The 4 requirements are sometimes conflicting in the sense that satisfying one condition may challenge another.

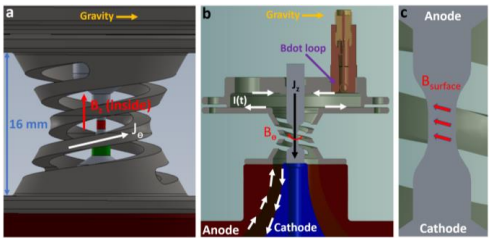

Figure 9. Field orientation generated by the HRC. (a) Orientation of current flow around the HRC, generating a positive axial field component. Note that the red-colored 1.00-mm-diameter surface can be fully viewed from 0° and 180° diagnostic lines of sight. (b) Orientation of current flow downward through the z pinch, generating a negative azimuthal field component. (c) Magnetic field orientation on the 1.00-mm-diameter surface of the z pinch, which is 15° rotated from horizontal (ϕ_B=15°) for the HRC shown. While the target is shown vertically, the Mykonos hardware is actually horizontally oriented. The direction of gravity is indicated in (a,b).

A variety of tools were used to evaluate HRC designs and select an optimal geometry. Diagnostic access (1) to the physics regions of interest were confirmed through CAD modeling (Fig 9(a)). The direction of current flow and associated field production for both the HRC and target are shown in Figs. 9(a,b),

resulting in polarized field at the rod's surface (Fig. 9(c)). Requirements (2, 3) concerning B_z production and axial gradients in field strength, $\partial B_z/\partial z$, were evaluated using the 3D Eulerian resistive MHD code KRAKEN, which solves the same electromagnetic equations as GORGON [lxxvii]. KRAKEN simulations driven with a 1-MA, 100-ns-risetime current pulse were used to evaluate both the axial and radial dependence of ϕ_B. First, simulations show that ϕ_B peaks at 15.1° at the axial center of the target and falls to 14.4° 0.5 mm above and below the axial center. Our experimental objective is to determine whether ~15° field polarization drives a ~15° rotation in ETI-driven heating patterns, therefore such 5% variation in field strength is deemed acceptable. Second, the diffusion of B_z and B_θ components into the metal are similar, resulting in constant ϕ_B when moving to smaller radius within the rod, as expected (see section 4.3 of [lxxviii]). By contrast, ϕ_B increases when moving to larger radius outside of the rod, since B_θ falls as 1/r whereas B_z is nearly constant.

Under ideal scenarios, the likelihood of helical shorting (4) has been evaluated through analytic estimates and ANSYS [lxxix] electromagnetic simulations. The HRC is designed with at minimum a ~3 mm gap between the inner surface of the HRC and the outer surface of the target. While this is sufficient to support the potential difference between these conductors, imperfect hardware alignment could reduce the gap locally, increase the electric field strength, and promote shorting. Shorting could also occur between helical conductors. While the HRC was conservatively designed with 2 mm vertical gaps between helical conductors, the HRC was quite flexible, and easily deformed, enabling smaller local gaps. Furthermore, the presence of hardware anomalies such as burrs, sharps, contaminants, and misalignments may drive unpredictable shorting behavior. In practice, we relied on previous experience in developing similar pulsed-field-production platforms such as AutoMag [lxxx, lxxxi] to guide our design. A discussion of hardware commissioning challenges (and solutions), including observations of current shorting and diagnostic vignetting, are discussed in Appendix 2.

Section V-c: Engineered defect (ED) target design

Engineered defect targets of the same "barbell" profile (Fig. 9) and general machining process as described in [lvi] were used in dynamic axial field experiments. Here, however, 4 ED pairs were included on the 0° and 180° sides of the target. All individual quasi-hemispherical ED were machined similarly, with rim diameter D_{rim}=24 µm and 6 µm center depth. Details of the patterns are shown in Fig 10(a). The 0° side of the target contains pairs of ED with center-to-center pair angle ϕ_{ED} of +0°, +7°, +11°, and +15° from horizontal. The 180° side contains angled pairs is of opposite slope (ϕ_{ED} of -0°, -7°, -11°, and -15°). The center-to-center spacing of each defect pair was 72 µm, regardless of ϕ_{ED}. The ϕ_{ED}=±0° pairs were nearest to the anode, while the ϕ_{ED}=±15° pairs were nearest to the cathode.

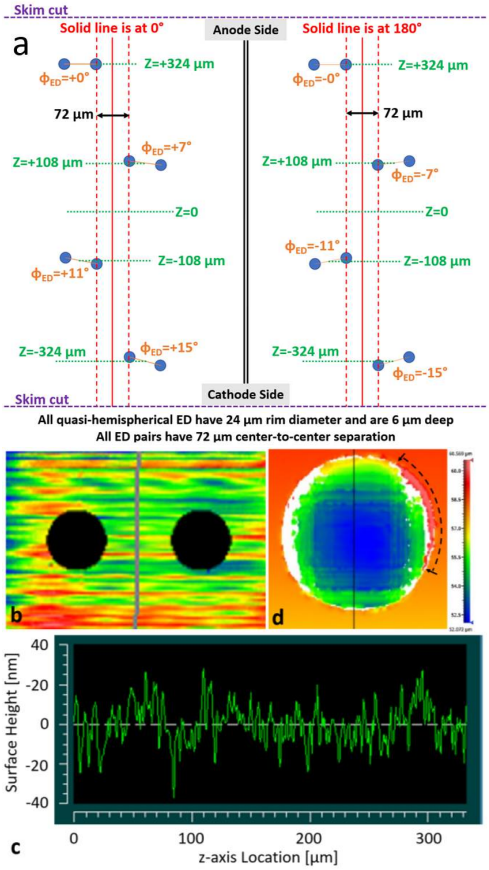

Figure 10. (a) ED pattern specification for experimental z pinch targets. (b) Interferogram of the azimuthally correlated machining grooves on surfaces near ED (the ED profiles have been masked as indicated by the black circles). (c) Surface height profile about the grey line in (b), extended, showing the height of surface machining grooves near ED (d) Interferogram of an ED, showing imperfections about the ED rim. White regions indicated data loss about locations of the ED where light reflection was insufficient for the measurement. The black dashed arc and arrows indicate the extent of a flap of material inside of the rim diameter and at nearly the same height as the nearby surface, which is likely a burr that was folded back over the ED rim rather than removed during the skim cut.

While world class machining tools and processes were applied to the fabrication of ED targets, surfaces remain imperfect. For surfaces near ED (Fig. 10(b, c)) the arithmetic mean roughness is typically quite near Ra=10 nm, with maximum peak-to-valley height about machining grooves of >50 nm (Fig. 10(c)). Furthermore, rims of ED are imperfect at the micron scale, and include both "chips" at the edge, as well as "folded over" burrs (Fig. 10(d)); such imperfections will impact surface heating. For example, micron-scale burrs have been shown [lvi] to drive the most rapid heating from similar ED (rather than following the vertically oriented polar heating pattern predicted for "perfect" ED). To eliminate the dominant influence of burrs, a "skim" cut procedure was implemented, where 500 nm of material was removed from the full surface after the ED were machined, but certainly some imperfections remain. Since we are

interested in subtle rotations of expected heating patterns due to changes in ϕ_B, *random* ED rim imperfection are likely to impact experimental results, presumably adding randomly oriented variability of unknown severity. Detailed analysis of the rim imperfections from a small sample of targets show that while all ED include rim imperfections, the locations and severity are not consistent. While some targets were left bare others were coated with Loctite UV-cure epoxy which was then diamond turned to a straight cylindrical surface of 35 µm thickness with no indentations above pits. See Appendix 4 for a detailed description of the dielectric coating fabrication and characterization process.

Section VI: Experimental results

Section VI-a: Bare/uncoated ED— Θ_{pole} rotation toward ϕ_B

Data obtained from *bare* (uncoated) ED targets with either ϕ_B=0°or ϕ_B=15° magnetic field polarization demonstrate that the ETI-driven polar heating about EDs aligns towards ϕ_B. For example, data from nominally identical targets are shown in Fig 11(a, b), where an SRC drove purely azimuthal field (ϕ_B=0°), or an HRC generated $\phi_B(t)$=+15°, respectively. Each ED overheats and emits brightly from upper and lower "poles;" when ϕ_B=0, these poles are predominantly vertically aligned (Θ_{pole}~0°, See Figs. 2,7), whereas these poles tend to rotate away from vertical for the $\phi_B(t)$=+15° experiment (Θ_{pole}~15°, See Figs. 3,7).

It is also apparent from Fig. 11 that the ED from a single experiment do not behave identically. For example, the emission intensity varies from one ED to the next, as does the polar emission strength from the two poles generated by a single ED. Importantly, the rotation angle of ED emissions, Θ_{pole}, observed from ED within a single experiment are also not identical. Such variability can be driven by micron-scale machining imperfections on or near the ED rim, and may also be impacted by the onset of plasma filaments which are known to form at a variety of angles within a single experiment, including angles much larger than 15° (see, for example, Fig. 3 of Ref. [xlix]). Given such variability, conclusions regarding ϕ_B's impact on polar rotation cannot be obtained from a single experiment. Rather, we evaluate Θ_{pole} from individual ED over many experiments to determine if ϕ_B has a statistically significant impact on Θ_{pole}.

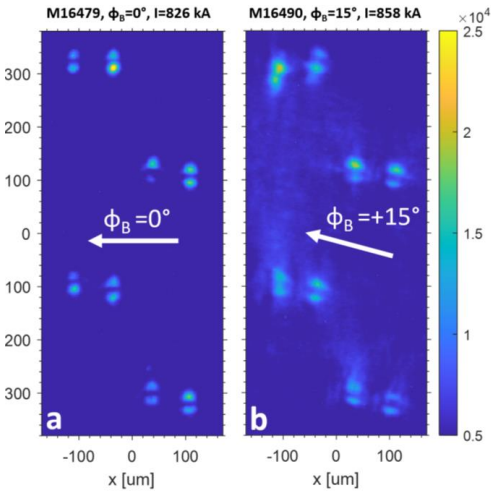

Figure 11. Self-emission images of uncoated ED targets, with common color bar [counts] for (a) ϕ_B=0° and (b) ϕ_B=15°. Images were gathered using model 334 or 340 Andor iStar intensified CCD cameras [lxxxii], sensitive to ~300-900 nm light, with the 340

camera having higher efficiency at shorter wavelengths. Questar QM100 long-distance microscopes are used to generate images. Images were gathered with ~3 ns gate width, and the spatial resolution at the object plane was at best 3 µm.

To determine Θ_{pole}, we locate the center coordinates of both poles generated by a single ED, and then calculate the angle of the line connecting the two pole centers. First a global rotation value (-2.0° for this image) is determined using the emissions from skim cut terminations (Fig. 12(a)), which are known to be horizontal. Next, emissions from each ED pair are isolated by generating 200X200 pixel "cropped" image arrays (e.g., red-dashed box in Fig. 12(a) leads to Figs. 12(b-d)). The background emission level far from the ED pair ("BKD") is found by averaging the counts in the 30X30 pixel areas about the corners of each image (black dashed squares, Fig 12(b)). Next, the cropped images are partitioned into 4 quadrants (white-dashed lines in Fig. 12(b)), to isolate each emission pole. The peak emission value is then found for each quadrant (e.g., $E_{peak,UL}$). Contour levels are then defined for each quadrant as the percent differences between BKD and the local quadrant peak. For example, the 90% contour for the UL quadrant is set at an emission level ($E_{UL,90}$) of: $E_{UL,90}$=BKD+0.90*($E_{peak,UL}$-BKD). Contour values of 25, 50, 75, 90, 95 and 99.5 percent are found. Note, that the contour values for each quadrant vary (e.g., $E_{UL,90} \neq E_{LL,90}$), but do match in a quasi-normalized sense in terms of percent difference between BKD and quadrant peaks.

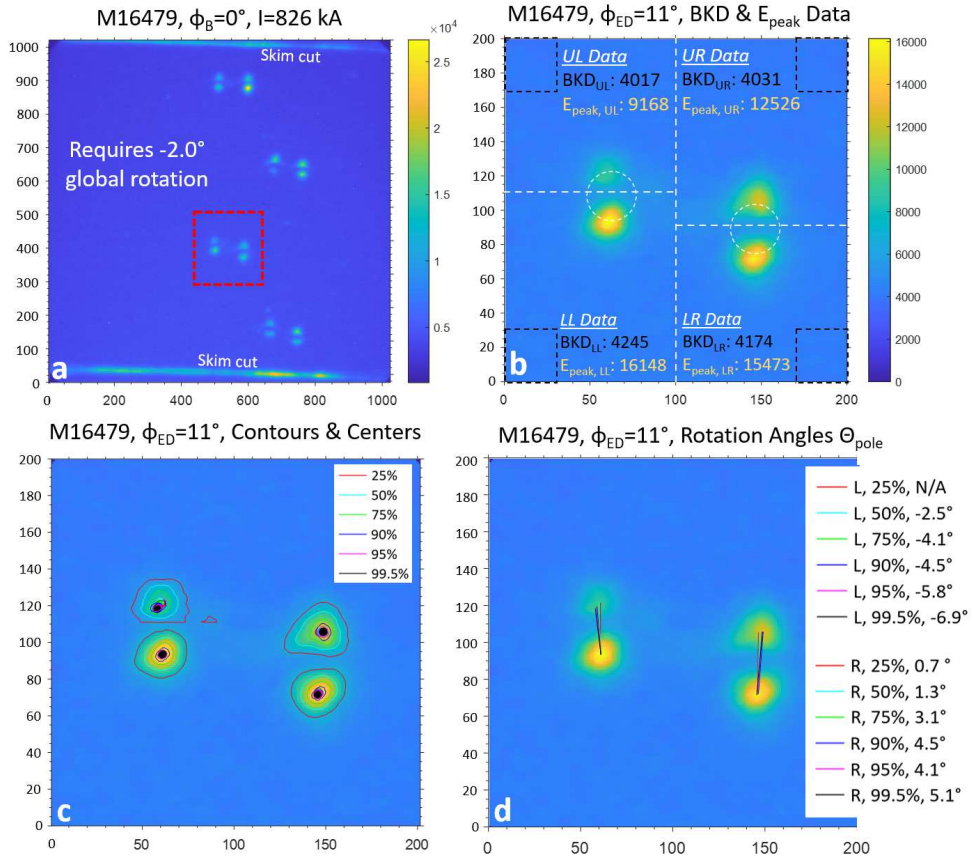

Figure 12: Image analysis procedure used to determine the pole rotation angle, Θ_{pole} for an experiment with ϕ_B=0°. All axes are in pixels. (a) Raw image, globally rotated, with a 5X5 median filter applied. (b) Cropped image of the ϕ_{ED}=11° pair from the red box in (a). (c) Overlay of contour boundaries used to find the "center-of-emission" points plotted in the same color. (d) Line connecting the centers of emission for the poles from each ED. Calculated Θ_{pole} values are reported in the legend. The final Θ_{pole} are then the sum of the angles shown in the (d) legend, and the -2° global image rotation specified in (a).

Contours are plotted in Fig 12(c). The x and y coordinates of the "center-of-emission" of all cells contained within each contour are then calculated by applying integrals which are mathematically equivalent to finding the center-of-mass of a limina of varying density per unit area. The angles versus vertical of the lines connecting the centers of similar-valued contours are found, as shown by the colored lines in Figure 12(d). The final Θ_{pole} are then the sum of the angles shown in the Fig. 12(d) legend, and the -2° global image rotation (Fig. 12(a)). Generally, in the results which follow, we discuss Θ_{pole} data gathered from the 90% contour, which lies well above the BKD emission level, but is of sufficiently low emission to avoid being dominated by very small-area local peaks. That said, the high-level conclusions to follow are qualitatively unchanged when evaluating rotation data from 75% through 99.5% contours.

Θ_{pole}, data from the 90% contours of 81 ED are included in Fig. 13, with 43 ED from ϕ_B=0° experiments and 38 ED from ϕ_B=15° experiments. Θ_{pole} measurements associated with each ED are color coded by ϕ_B, and separately by whether data originates from the L or R ED within a pair (see legend). 15 of the 16 combinations of ϕ_B, ϕ_{ED}, and (L or R) are represented in the plot (no ϕ_B=15°, ϕ_{ED}=0°, L emission data were gathered which were compatible with the analysis method). The fifth panel combines data from all pair angles and presents 4 averages (with 1 standard deviation presented as error bars) for the four primary cases: (ϕ_B=0°||L), (ϕ_B=0°||R), (ϕ_B=15°||L), (ϕ_B=15°||R).

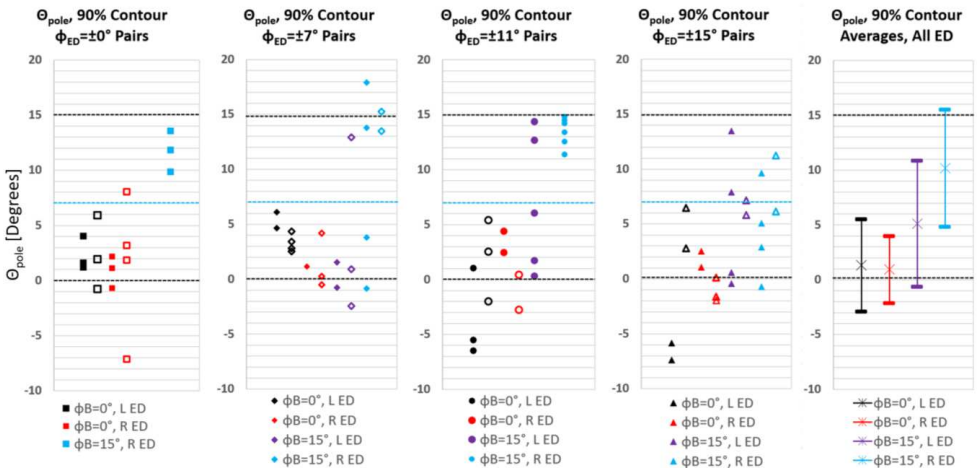

Figure 13: Pole rotation angle, Θ_{pole}, for 90% contours from 81 ED. Data are plotted within separate panels according to the absolute value of pair angle, ϕ_{ED}, where positive ϕ_{ED} are plotted with filled markers, negative ϕ_{ED} are plotted with hollow markers of the same shape and color. Black, red, purple, and blue data points are associated, respectively, with the following four cases: (ϕ_B=0°||L), (ϕ_B=0°||R), (ϕ_B=15°||L), and (ϕ_B=15°||R), where L and R indicate which ED Θ_{pole} was calculated from. The fifth panel averages data for these four cases, where the center point gives $\Theta_{pole,AVG}$ with 1 standard deviation "error bars" assigned. Note that the x-value of data points has no physical meaning. Data are simply horizontally separated within panels to avoid excessive overlap.

Several conclusions can be drawn from the data in Fig. 13. First, ϕ_{ED} has no clear impact on Θ_{pole}, which is expected, since bare ED are known to evolve largely in isolation throughout the time of surface plasma

formation. Next, despite the spread contained within this limited dataset, ϕ_B does significantly influence Θ_{pole}. As shown in the 5th panel of Fig. 13, $\Theta_{pole,AVG}$ ~1° for ϕ_B=0° for both left and right ED whereas when ϕ_B=15°, $\Theta_{pole,AVG}$ =5° for left ED and $\Theta_{pole,AVG}$ =10° for right ED. To determine whether the observed difference between the means of these datasets is statistically significant, we apply Welch's t-test [lxxxiii], and separate the data in Fig. 13 into two groups. Group one includes 43 Θ_{pole} datapoints for ϕ_B=0° (black and red datapoints), and the second includes 37 Θ_{pole} datapoints for ϕ_B=15° (purple and blue datapoints). The null hypothesis that the mean polar angles for the two datasets are equal is rejected, as indicated by the hypothesis test result, h=1. The p-value, p=0.0000 indicates very strong evidence against the null hypothesis. Furthermore, the test indicates that the difference in the mean of the ϕ_B=15° and ϕ_B=0° datasets falls within the range from 4.6° to 9.1° degrees with 95% confidence. To further exemplify the impact of ϕ_B, note that only 1 out of 43 ϕ_B=0° ED emissions have Θ_{pole}>7° (Θ_{pole}=7° indicated by blue dashed lines), whereas 21 out of 38 ϕ_B=15° ED emissions have Θ_{pole}>7°. However, it is noteworthy that, $\Theta_{pole,AVG}$ for ϕ_B=0° is nearly 0°, matching prediction, whereas $\Theta_{pole,AVG}$ for ϕ_B=15° is much less than 15° (falling well below the theoretical prediction). Several experimental factors could influence this inconsistency. First, the azimuthally correlated orientation of background machining grooves (see Fig. 10(b)), would likely tend to favorably align pole heating towards the vertical (Θ_{pole} near 0°). Second, it is possible that ϕ_B did not meet the experimental design specification of 15° due to undetected temporally and spatially variable shorting. Finally, incomplete understanding of the governing physics may remain.

The observed difference in Θ_{pole} data for left versus right ED for ϕ_B=15° experiments was unexpected and is not yet understood. That said, one potentially impactful machining asymmetry was uncovered after the experiments and is discussed in Appendix 3.

Section VI-b: Dielectric coated ED—Pair merging along ϕ_B

Data obtained from *dielectric-coated* ED targets demonstrate both local alignment of overheating patterns from single ED towards ϕ_B and enhanced merging for ED pairs when ϕ_{ED} is aligned with ϕ_B. For example, data from nominally similar targets are shown in Fig. 14. The left-hand column (Figs. 14(a-d)) displays data from experiment M16523 where ϕ_B=0° (compare to Fig. 5) while the right-hand column (Figs. 14(e-h)) displays data from experiment M16502 where ϕ_B=+15° (compare to Fig. 6). Here, we display emissions from the ϕ_{ED}=+15° pairs (Figs. 14(a,e)), the ϕ_{ED}=0° pairs (Figs. 14(b,f)), and the ϕ_{ED}=-15° pairs (Figs. 14(c,g)). It is apparent that the pair heating topography changes with ϕ_B. For example, when considering the ϕ_B=0° data, the ϕ_{ED}=0° pair (Fig. 14(b)) demonstrates well-connected emission about the 0° straight line connecting the ED centers, while emissions between the ϕ_{ED}=+15° and ϕ_{ED}=-15° pairs (Figs. 14(a) and 14(c)) are more segmented. Similarly, when considering the ϕ_B=+15° data, the ϕ_{ED}=+15° pair (Fig. 14(e)) demonstrates well-connected emission about the +15° straight line connecting the ED centers, while emission between the ϕ_{ED}=0° and ϕ_{ED}=-15° pairs (Figs. 14(f) and 14(g)) become progressively more segmented as the misalignment between ϕ_{ED} and ϕ_B grows. Thus, data are consistent with preferred merging about ED pairs which are well aligned to ϕ_B. Next, we quantify these qualitative observations by evaluating (1) how ϕ_B alters local overheating orientation from individual ED, (2) pair merging connectivity as a function of the difference in angle between ϕ_B and ϕ_{ED}, and (3) the evolution of pair merging as a function of target current for various ϕ_B to ϕ_{ED} alignment.

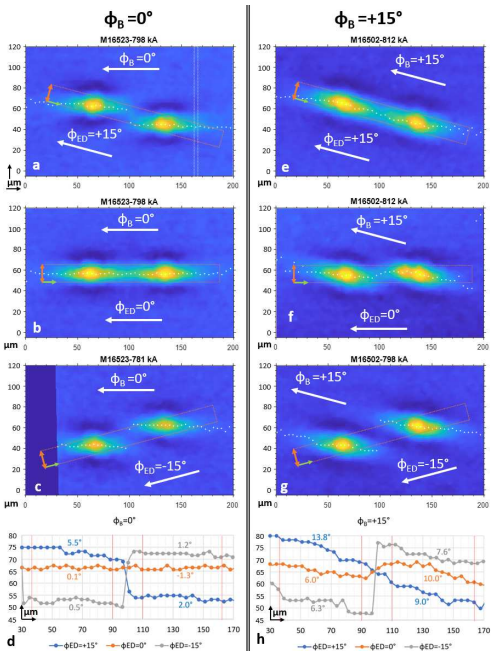

Figure 14: Data on pair merging and local emission rotation for ϕ_{ED}=+15°, 0°, and -15° pairs for the cases of ϕ_B=0° (a-d) and ϕ_B=+15° (e-h). Both ϕ_{ED}=0° and ϕ_{ED}=+15° pairs were on the 0° side of the target, while the ϕ_{ED}=-15° pairs were on the 180° side of the target. Therefore, images were captured with separate ICCDs at different times and the load currents differ minimally. Localized ED emissions from individual ED are ellipse-like, with a major axis that tends to align toward ϕ_B. To quantify these observations, the location of peak emissions from 5-pixel wide vertical profiles (e.g., white rectangle in (a)) were superimposed on the image, generating the series of white circles. These data are replotted in (d) and (h). Angles reported in (d) and (h) correspond to the major axis of each ellipsoid.

The data in Fig. 14 show that ϕ_B alters the local overheating orientation of an individual ED. While pair merging is apparent and thus individual ED do not evolve in full isolation, it is nonetheless true that each ED develops local ellipse-like emission, and the major axis of these ellipse-like emissions tends to align toward ϕ_B. To quantify this effect, vertical profiles were obtained by segmenting each image into 5-pixel-wide, full-height rectangles (see the example white rectangle in Fig. 14(a)). For each profile, the maximum was found, and the z-location of that maximum was plotted over the image, generating the series of white circles shown in Figs 14 (a-c & e-g). Curves generated in this manner are replotted together in Figs. 14(d & h). The data confirm that the most continuous straight-line emissions connecting the ED centers occurs for $\phi_{ED}=\phi_B$ (compare the orange curve in Fig. 14(d) and blue curve in Fig. 14(h) to $\phi_{ED}\neq\phi_B$ curves within each plot). Furthermore, linear fits have been determined for the portions of the curves nearest the center of each ED. Linear fits are derived from the data points within the vertical red lines pairs in plots 14(d) and 14(h), which span about 2X the original rim diameter of the ED and provide an estimate of the angle of the major axis of each ellipsoid. Here, we see that major-axis angles of the ellipsoids associated with ϕ_B=0° are small in comparison to the major-axis angles associated with the ϕ_B=+15°, suggesting favorable orientation of local heating patterns along ϕ_B.

Next, we evaluate pair merging strength for varying ϕ_B to ϕ_{ED} alignment. To do so, emission profiles are calculated along straight lines passing through the center of each ED within a pair (i.e., along an angle ϕ_{ED}). Data contained within the orange rectangles shown in Fig. 14(a-c & e-g) are averaged about the 20-cell "height" (along the orange double arrows) and plotted along the axis indicated by green arrows. Profiles are normalized by setting the peak emission associated with the center of the brightest ED to 1 and the average background emission associated with surface emission far from the ED pair to zero. Fig. 15(a) displays these profiles for experiment M16523 where ϕ_B=0° while Fig. 15(b) displays profiles from experiment M16502 where ϕ_B=+15°.

Emissions between ED pairs, centered at 0 μm on the x-axis, are shown to increase as the difference in angle between ϕ_{ED} and ϕ_B falls, as indicated by the emission profiles in Fig. 15. In Fig 15(b), where ϕ_B=+15°, the emission profile for the ϕ_{ED}=-15° pair (30 degrees different from ϕ_B) falls to the background level (near zero scaled emission), whereas emissions from the ϕ_{ED}=+15° pair (ϕ_{ED}=ϕ_B) is strongest at 40% of the scaled peak value, indicative of stronger pair merging. The trend is largely followed, where better alignment between ϕ_{ED} and ϕ_B results in stronger pair merging. The data in Fig 15(a), where ϕ_B=0°, shows a similar trend, with the strongest pair merging observed for those pairs where ϕ_{ED}=ϕ_B (ϕ_{ED}=±0° in this case), with lowest merging for the most poorly aligned pairs (ϕ_{ED}=±15° pairs in this case). Here, no inter-ED heating profiles fall to the background level, apparently due to the reduced maximum misalignment between ϕ_{ED} and ϕ_B. Trends in pair merging strength are summarized in Fig. 15(c), where profile minima near x=0 (found by fitting a parabola to each curve using data from -20 μm to +20 μm) have been plotted against their respective ϕ_{ED} for all curves in Figs. 15(a,b). For ϕ_B=0°, pair merging strength peaks for ϕ_{ED}=±0° and falls as the difference between ϕ_B and ϕ_{ED} grows. By contrast, for ϕ_B=15° pair merging is weakest at ϕ_{ED}=-15° and increases as ϕ_{ED} grows.

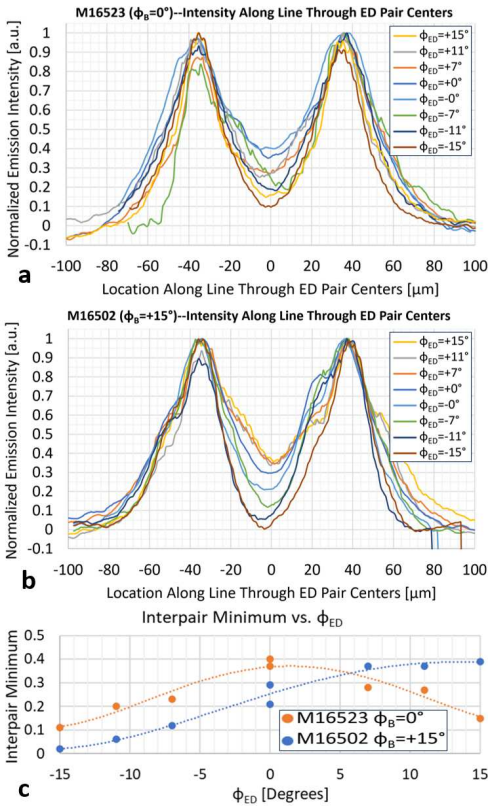

Figure 15. Emission profiles which enable evaluation of pair merging strength for varying ϕ_{ED} to ϕ_B alignment. Profiles are plotted separately for each of the 8 ED pairs from experiments (a) M16523 (ϕ_B=0°) and (b) M16502 (ϕ_B=+15°). For (a), ϕ_B=0°, the ϕ_{ED}=±0° curves have the strongest central emission between the two ED (strongest merging), while the central emission level falls for progressively larger $|\phi_{ED}|$. For (b), ϕ_B=+15°, the ϕ_{ED}=+15° curve shows strongest merging, with weaker merging for smaller values of ϕ_{ED}. Trends in pair merging strength are summarized in (c), where the minima near x=0 have been plotted against their respective ϕ_{ED} for all curves in (a) and (b). Orange and blue trendlines, intended only as guides, are 4th order polynomial fits to each dataset.

Finally, we evaluate how the strength of pair merging changes with increasing current for varying ϕ_{ED} to ϕ_B alignment by comparing data gathered from multiple experiments, at different currents. Profiles are obtained using similar processing as that used to generate Fig. 15. In Fig. 16(a), $\phi_{ED}=\phi_B$=+15° (dashed) and $\phi_{ED}=\phi_B$=0° (solid) profiles are plotted. The degree of pair merging increases with current, reaching a maximum (normalized) value near 0.5. It is noteworthy that the degree of merging appears nearly identical for the two $\phi_{ED}=\phi_B$=0° and $\phi_{ED}=\phi_B$=+15° datasets (compare dashed/solid curves of comparable Mykonos current), suggesting ϕ_{ED} to ϕ_B alignment is the primary driver of the merging rate for closely spaced ED pairs. In Fig. 16(b), ϕ_B=+15°, ϕ_{ED}= 0°, (dashed) and ϕ_B=0°, ϕ_{ED}=+15° (solid) profiles are plotted for the same set of experimental images and currents. The tendency for pair merging to increase at larger current again generally holds, but, given that ϕ_B and ϕ_{ED} are misaligned by 15° in all cases, pair merging is reduced overall versus the data in Fig. 16(a), with the maximum normalized emission between pairs (at

highest current) reaching only about 0.3. Trends in pair merging strength versus current for the various ϕ_B and ϕ_{ED} combinations are summarized in Fig. 16(c), where profile minima (found by fitting a parabolas to each curve using data from -20 μm to +-20 μm) have been plotted against their respective Mykonos current for all curves in Figs. 16(a,b). Separate curves are plotted for the 4 combinations of ϕ_B=0°,+15° and ϕ_{ED}=0°,+15°. Profile minima are higher when $\phi_B = \phi_{ED}$ than when these parameters differ by 15° and in all cases merging strength increases with current. These data strongly support that for a randomized distribution of current density perturbations on a dielectric coated conductor, nearby perturbations will favorably merge about ϕ_B, with the degree of merging increasing with current.

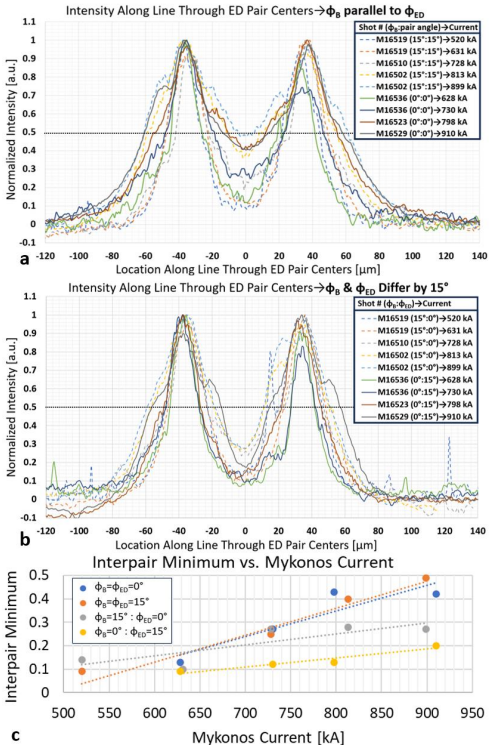

Figure 16. Pair merging as a function of current for varying ϕ_{ED} to ϕ_B alignment. Data in (a) are profiles for ϕ_{ED} parallel to ϕ_B for both $\phi_{ED}=\phi_B=0°$ (solid lines) and $\phi_{ED}=\phi_B=15°$ (dashed lines). Data in (b) are profiles where ϕ_{ED} and ϕ_B differ by 15° (see legend). Trends in pair merging strength are summarized in (c), where the inter-pair minima have been plotted against their respective Mykonos current for all curves in (a,b). Color-coded trendlines, intended only as guides, are linear fits to each dataset.

Section VII: Concluding remarks

Experiments demonstrate rotation of electrothermal instability (ETI)-driven overheating structure from 10-micron-scale ED machined into the surface of aluminum z pinch rods which were pulsed with helically-polarized surface magnetic field. Experiments were either of a standard z pinch configuration, with B_z=0, or used a HRC to generate dynamically rising surface magnetic field at a field polarization angle ϕ_B= 15° (from horizontal). 8 ED pairs were machined into each target with pair angles, ϕ_{ED}, of ±0°, ±7°, ±11°, and

±15° (0° and 180° sides of the target contain positive and negative ϕ_{ED}, respectively). Some targets were left bare while others were coated with 35 μm of Loctite UV-cure epoxy.

For bare targets, surface plasma forms before significant ED pair merging occurs; therefore, heating topography is studied from individual ED (prior to plasma formation), after ETI overheating has generated strong emission from the ED poles. Analysis focused primarily on whether the polar heating angle, Θ_{pole}, from individual ED rotated toward ϕ_B. As expected, Θ_{pole} was not dependent on ϕ_{ED}. However, data clearly indicate that ϕ_B does influence Θ_{pole} with $\Theta_{pole,AVG}$ ~1° for ϕ_B=0° whereas when ϕ_B=15°, $\Theta_{pole,AVG}$ reached 5° to 10°. Application of Welch's t-test confirms that the observed difference in Θ_{pole} for the ϕ_B=0° versus ϕ_B=15° datasets is statistically significant, indicating that the difference in the mean Θ_{pole} falls within the range from 4.6° to 9.1° degrees with 95% confidence. These data show that individual, 10-micron-scale current density perturbations will heat and explode with an orientation governed by the helicity of the applied surface field, demonstrating the generation of a helically oriented seed for the helical instabilities observed in axially magnetized z pinch experiments.

The addition of a dielectric coating changes the hydrodynamic evolution of the underlying metal, which delays surface plasma formation, allowing extended study of the development of ETI strata. This enables observation of the merging of overheating structures within ED pairs. The dielectric-filled and coated EDs studied here may evolve similarly to subsurface resistive inclusions, which also divert current while being tamped hydrodynamically by overlying material and furthermore provide data relevant to MagLIF liner implosions which employ similar dielectric coatings to mitigate instability development. Data demonstrate both local alignment of overheating patterns about ϕ_B and enhanced merging for ED pairs when ϕ_{ED} is aligned to ϕ_B. Emissions between ED pairs are shown to increase (enhanced pair merging) as the difference in angle between ϕ_{ED} and ϕ_B falls. Data further demonstrate that for ED pairs where ϕ_{ED}=ϕ_B the degree of pair merging increases with current, with the degree of merging being nearly identical for the two ϕ_{ED}=ϕ_B=0° and ϕ_{ED}=ϕ_B=+15° datasets, suggesting ϕ_{ED} to ϕ_B alignment is the primary driver of the merging rate for closely spaced ED pairs. For instances where ϕ_B and ϕ_{ED} are misaligned by 15°, pair merging is reduced overall, including at high current. These data strongly support that for a randomized distribution of current density perturbations on a dielectric coated conductor, nearby perturbations will favorably merge about ϕ_B, with the degree of merging increasing with current. For many closely spaced perturbations, reasonable extension of these observations leads to the ETI-driven formation of elongated structures which are preferentially aligned towards ϕ_B.

Such observations demonstrate that in thick metals (i.e., current carrying skin depth much smaller than the metal's thickness) subject to dynamic axial magnetic field $B_z(t)$, the orientation of ETI-driven runaway heating is dictated by the surface field polarization angle ϕ_B, largely in agreement with 3D MHD simulations. Together, these results offer fundamental new understanding of the seeding mechanisms of the helical magneto-Rayleigh Taylor (MRT) instabilities observed from magnetically-driven imploding liners when driven by dynamic $B_z(t)$. In the case of static B_z, as in the MagLIF concept, MHD simulations again predict helically asymmetric ED emission, but the physical mechanism is very different. These simulation predictions will be tested in a future experimental campaign.

Acknowledgements

The authors would like to acknowledge useful conversations with and/or support from D. Ampleford, P. Ballance, B. Bauer, S. Bova, E. Breden, K. Cochrane, A. Crabtree, M. Cuneo, K. DeZetter, M. Gilmore, I. Golovkin, E. Harding, N. Hines, T. Hutchinson, B. Hutsel, D. Jaramillo, C. Jennings, M. Jones, C. Kalogeras, I. Kern, D. Lamppa, W. Lewis, L. Lucero, K. Matzen, J. Niederhaus, R. Obregon, R. Paguio, L. Perea, K. Perkins, K. Peterson, M. Rich, A. Robinson, G. Rochau, K. Rodgers, A. Sarracino, J. Schwarz, D. Sinars, S. Slutz, R. Speas, S. Speas, A. Steiner, W. Tatum, R. Vesey, M. Weis, and D. Yager-Elorriaga. This research

was supported by Sandia's Laboratory Directed Research and Development Program (LDRD, Project Nos. 200269 and 229427). This work was also funded in part by Sandia's LDRD program via the appointment of one of the authors (G. Shipley) to the Truman Fellowship in National Security Science and Engineering, Project No. 226067. Sandia National Laboratories is a multi-mission laboratory managed and operated by National Technology and Engineering Solutions of Sandia, LLC., a wholly owned subsidiary of Honeywell International, Inc., for the U.S. Department of Energy's National Nuclear Security Administration under Contract No. DE-NA-0003525. This paper describes objective technical results and analysis. Any subjective views or opinions that might be expressed in the paper do not necessarily represent the views of the U.S. Department of Energy or the United States Government

AUTHOR DECLARATIONS

Conflict of Interest

The authors have no conflicts to disclose.

Author Contributions

T. J. Awe: Conceptualization, Data Curation, Formal Analysis, Funding Acquisition, Investigation, Methodology, Project Administration, Validation, Visualization, Writing/Original Draft Preparation, Writing/Review & Editing
E. P. Yu: Conceptualization, Formal Analysis, Investigation, Methodology, Visualization, Writing/Original Draft Preparation
G.A. Shipley: Conceptualization, Formal Analysis, Funding Acquisition, Investigation, Methodology, Visualization
K. C. Yates: Conceptualization, Data Curation, Investigation
K. Tomlinson: Conceptualization, Investigation, Methodology, Resources
M. W. Hatch: Conceptualization, Methodology

Data Availability

The data that support the findings of this study are available from the corresponding author upon reasonable request.

Appendix 1: Simulation details

ALEGRA (Arbitrary Lagrangian-Eulerian General Research Application) is a finite element computer code developed at Sandia National Laboratories since 1990. For the applications discussed in the manuscript, ALEGRA solves the resistive MHD equations (displacement currents are neglected in Maxwell's equations), including Ohm's law $\eta \boldsymbol{j} = \boldsymbol{E} + \boldsymbol{v} \times \boldsymbol{B}$ (Hall term is not incorporated). For specifics on the equations solved by ALEGRA, please see [lxxxiv]

The periodic wedge simulations use a curvilinear cylindrical Eulerian mesh centered at the origin in (x,y) and aligned along the z axis. High resolution (0.5 μm) cells are used near ED to properly resolve the current redistribution there.

ALEGRA allows for vacuum regions (i.e., zero mass density) surrounding the metal rod, but to keep the magnetic solve tractable, a finite electrical conductivity σ_V (equal to the maximum electrical conductivity in the mesh divided by 10^7) is assigned to the vacuum. While finite σ_V allows a small fraction of total current (<0.01%) to flow in vacuum, the vacuum cells are otherwise not permitted to participate in the physics.

The dielectric electrical conductivity table (lxn29742) was created using density functional theory calculations by Thomas Mattsson and Michael Desjarlais. The dielectric electrical conductivity σ_d rises with increasing temperature and (especially) density, although over the course of the simulation, the increase in temperature is only 11 Kelvin. Despite this modest temperature increase, the combination of compression and heating in the dielectric results in a 100X increase in σ_d. Coupled with a 100X decrease in σ in the metal (due to Joule heating), we might expect the dielectric to eventually carry significant current, but in fact σ_d remains 11 orders of magnitude lower than in the metal. Hence, current remains in the metal and the dielectric serves primarily as a mass tamper. Dielectric breakdown is not treated in these simulations, nor do we expect breakdown to occur for the electric fields experienced by these targets.

Appendix 2: Platform commissioning challenges and solutions

Two significant hardware changes were required to add dynamic B_z to the ED platform. New powerflow hardware was developed (Fig. 8) to reduce inductance and enable connection to a new HRC (Figs. 8,9) to apply dynamic helical field to the z pinch target. This new hardware includes closely spaced conductors at significant potential difference which increases the risk of current shorting. Magnetic "Bdot" probes were fielded both upstream of the MITL (standard Mykonos "Machine" Bdots, located in a radial transmission line directly below the coaxial feed of Fig. 8) and downstream of the target region ("load" Bdots placed in the anode cap of the HRC-target assembly, see Figs. 8,9). Comparing the I(t) inferred from upstream/downstream Bdots clearly indicates whether MITL/target-region shorting occurred. For example, Bdot traces from experiments M15991 and M15999 are shown in Fig. 17(g). M15991 demonstrate uninterrupted current delivery through the load region, as indicated by the largely overlapping machine (black, solid) and load region (black dashed) Bdot curves. By contrast, M15999 data display early current shorting as indicated by the collapse of the load region Bdot traces (red, dashed) before the machine current (red, solid) reached 50 kA. Note also the higher dI/dt of the machine current in the instance of current shorting, due to the machine driving a lower inductance system after shorting occurs.

Shorting was attributed to two likely causes, both associated with the HRC. First, the "as machined" HRCs contained burrs and sharps (Fig 17(a)), which would promote local field enhancement. These features were eliminated by aggressive bead blasting all HRC surfaces (Figs 17(c,d)) using a Clemco Zero model (BNP-55S 600 CDC 115/1/60) bead blaster with glass oxide media (CAS #: 65997-17-3). After bead blasting, the HRCs were washed with warm soapy water, rinsed with warm water, and further rinsed with ethyl alcohol. Second, the flexible nature of the HRC resulted in the accordion-like compression of one side of the structure, reducing the gap between neighboring helices, and also de-symmetrizing the gap between the target and HRC. This problem was exacerbated by the horizontal orientation of the load assembly (Fig. 8), particularly when hanging Bdots and cables from the anode cap of the HRC-target assembly. Such asymmetric compression was eliminated by adding peripheral insulating jackscrew supports outside of the HRC conductors (Fig. 17(e)). After deploying bead blasting, and adding the peripheral supports to the 15° HRCs, 13 experiments were fielded, none of which generated Bdot data indicative of shorting.

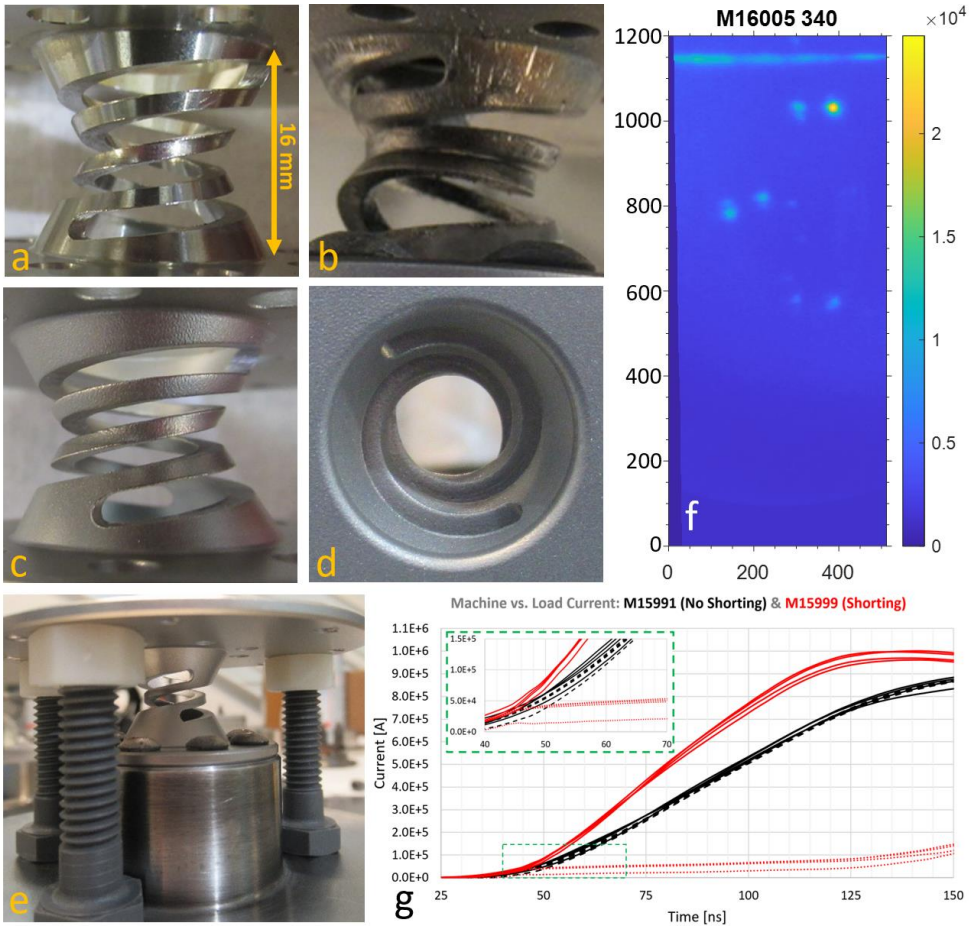

Figure 17. HRC platform commissioning. (a) As-received HRC with local sharps and burrs. (b) HRC after an experiment, in an instance where strong current shorting was observed. It is noteworthy that in all 3 experiments where catastrophic shorting was indicated by the Bdot data, the HRC survived the experiment (although it was deformed, as in (b)) while in all experiments where shorting was not indicated, the helical conducting paths were vaporized. This indicates that the current flowed through the helices in the absence of shorting, but either didn't reach the HRC or was supported by some other adjacent plasma in cases of appreciable shorting. (c) Side view of an HRC after bead blasting. Sharps and burrs have been removed. (d) Top-down view through the center of an HRC after bead blasting. (e) View of peripheral insulating "jack screws" which were used to eliminate the accordion-like compression of the flexible HRC, thus preserving uniform inter-helix gap spacing. (f) ICCD image from an experiment where reduced HRC gaps resulted in data loss due to aperturing and vignetting of the experimental image. Axes in pixels. (g) Current versus time curves generated from Bdot probes upstream (solid) and downstream (dashed) of the HRC for an experiment where no shorting was observed (black) versus an experiment where strong shorting was observed (red).

Shot to shot variations in HRC asymmetry and alignment also impact self-emission imaging data quality. As shown in Fig. 9(a), to enhance field production, the HRC included an interhelix gap just large enough to enable diagnostic access to the full central height of the 1.0 mm diameter portion of the barbell. While

this design enabled a view of all 4 defect pairs on a given side of the target, in practice, achieving adequate HRC alignment to enable unimpeded diagnostic access to the target proved quite challenging. The HRC sometimes completely blocked data from one or two ED pairs. For example, self-emission data from the Andor 340 camera in experiment M16005 (Fig 17(f)) captures emission from only 3 of the 4 defect pairs, and image contrast was poor. In instances of marginal misalignment, while emissions from all ED pairs are captured, axial gradients in emission intensity are observed, presumably due to vignetting. The addition of the peripheral support structures used to eliminate inter-helix shorting (Fig. 17(e)) had a secondary benefit of reducing vignetting, but variable and uncharacterized diagnostic aperturing from one shot to the next persisted. As a result of these uncharacterized changes in diagnostic access to the emitting region of the target, ICCD counts are not a reliable indicator of target emission intensity, and quantities should not be compared across experiments. However, topographic data from images, including shapes, profiles, and rotations/orientations of ED emissions are unaffected by such changes in diagnostic sensitivity, and can be meaningfully compared across images, after normalization.

Appendix 3: Left-right machining asymmetry

The observed difference in Θ_{pole} for left versus right ED for ϕ_B=15° experiments (Section VI-a, Fig. 13) was unexpected and is not yet understood. That said, one potentially impactful machining asymmetry was uncovered after the experiments. All ED are machined individually, using a 5-axis lathe configured in slow tool servo mode. Here, the target rotates slowly, while a specifically profiled diamond tool scoops out the ED layer by layer, until achieving the final ED profile and depth. The tool always enters from the right side of the ED, and exists from the left. In doing so, the rake angle, α of the tool enters the cut at positive 27° and exits at -27° (Figs. 18(a,b)). Positive rake angles provide a sharper cutting angle; thus, we expect the roughness of each ED to be smaller at the entrance of the ED versus the exit. For an ED pair, where the current density is slightly higher in between the pair (Fig. 18(c)), the right ED will have the rougher surface towards the higher j amplification (see Fig. 1 and discussion), whereas the left ED will have its smoother surface towards the higher j amplification. We offer this discussion of machining asymmetry only as speculation, not a claim of causality, as we don't have detailed data on the variation in ED roughness in these regions, where light return to the white light interferometry diagnostic used to gather surface topography information is poor.

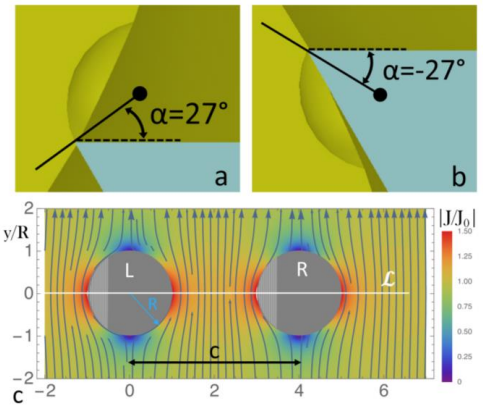

Figure 18. Discussion of a target asymmetry that could possibly explain the observed difference in Θ_{pole} for left and right ED. (a) and (b) show the changing rake angle, α, of the diamond cutting tool as the ED is cut. The solid black line connects the center of

the full sphere (black dot) associated with the quasi-hemispherical ED to the tip of the diamond tool. The dashed line defines the cutting edge of the tool. (c) Corrugated patterns have been added to the ED within the flow field (see Fig. 1 and discussion) to crudely denote which side of the defects are rougher due to the machining process, highlighting the source of possible experimental asymmetry.

Appendix 4: Dielectric coating fabrication and characterization

Select ED targets were overcoated with dielectric epoxy which was then diamond turned to a straight cylindrical surface (no indentations above pits) of 35 µm thickness. To meet the needs of the experiment, the epoxy must be optically clear so the metal surface below can be viewed both during pre-shot characterization and in experimental images. It is also critical that a bubble-free coating can be generated so that the mass tamping properties are uniform. Loctite 4311 UV-cure epoxy [lxxxv] (Ethyl cyanoacrylate with photoinitiator) was found to meet these requirements.

The dielectric layer was fabricated through the following procedure. Upon completing the machining of the metal surface of the target (surface profile and ED) the target remains in the lathe. A drop of epoxy is applied to the tip of an optical fiber, which is used as an applicator. The epoxy is examined using high magnification microscopy to ensure no air bubbles are present. The lathe then rotates the target at approximately 100 RPM while epoxy is applied to the central 1.00-mm-diameter portion of the target and cured using a handheld UV light source for 90 seconds. After curing, epoxy surface is single point diamond turned to the desired diameter.

The fabrication process outlined above assures that the thickness of the coating is precisely controlled. So long as the final turning of the Loctite outer diameter is machined to the programmed radius without ever removing the metal target from the lathe, the sub-micron accuracy of the machine's linear movements ensure that the coating thickness nearly exactly matches the programmed value. Nonetheless, the dielectric thickness of each target was checked using a Zygo NV7300 interferometric surface profiler with a built in "thin film" application. The tool calculates the film thickness using Loctite's index of refraction, IR=1.5, and scanning through the film to the underlying surface.

To validate this method, we developed a test part which enabled an independent check of the epoxy's IR. We diamond turned a test rod to a diameter of 1.00 mm. Half the rod (axially) was coated with a 35-µm-thick layer of epoxy using the fabrication steps detailed above. The resulting object include a section of bare metal, directly adjacent to coated metal. The height of the epoxy could then be checked via two methods. First, we checked the step height on a Zygo interferometric surface profiler by comparing the radial height of the Loctite versus the neighboring bare metal (i.e., not looking through the Loctite). The result matched the 35 µm dielectric thickness prescribed by the machining process, confirming the sub-micron accuracy of the machining movements. Finally, we used the Zygo thin film application to look through the Loctite (the method required to inspect the actual experimental targets). With the IR parameter set to 1.0, a 53 µm thickness was calculated. Adjusting the IR parameter to 1.5 resulted in the correct thickness of 35 µm, confirming the previously assumed IR value. Each subsequent load was inspected using an IR value of 1.5.

References

[i] I. R. Lindemuth, Two-dimensional fiber ablation in the solid-deuterium Z pinch, Phys. Rev. Lett. 65, 179 (1990).
DOI: https://doi.org/10.1103/PhysRevLett.65.179

[ii] J.E. Hammel, D.W. Scudder, J.S. Shlachter, Recent results on dense Z pinches, Nuclear Instruments and Methods in Physics Research, Volume 207, Issues 1–2, 1983, Pages 161-168, ISSN 0167-5087, DOI: https://doi.org/10.1016/0167-5087(83)90233-8

[iii] U. Shumlak; Z-pinch fusion. *J. Appl. Phys.* 127, 200901 (2020). DOI: https://doi.org/10.1063/5.0004228

[iv] J.E. Bailey, G. A. Chandler, S. A. Slutz, G. R. Bennett, G. Cooper, J. S. Lash, S. Lazier, R. Lemke, T. J. Nash, D. S. Nielsen, T. C. Moore, C. L. Ruiz, D. G. Schroen, R. Smelser, J. Torres, and R. A. Vesey, X-Ray Imaging Measurements of Capsule Implosions Driven by a Z-Pinch Dynamic Hohlraum, Phys. Rev. Lett. 89, 095004 (2002). DOI: https://doi.org/10.1103/PhysRevLett.89.095004

[v] A. L. Velikovich, R. W. Clark, J. Davis, Y. K. Chong, C. Deeney, C. A. Coverdale, C. L. Ruiz, G. W. Cooper, A. J. Nelson, J. Franklin, L. I. Rudakov, Z-pinch plasma neutron sources. *Phys. Plasmas*, 14, 022701 (2007). DOI: https://doi.org/10.1063/1.2435322

[vi] C. A. Coverdale, C. Deeney, A. L. Velikovich, R. W. Clark, Y. K. Chong, J. Davis, J. Chittenden, C. L. Ruiz, G. W. Cooper, A. J. Nelson, J. Franklin, P. D. LePell, J. P. Apruzese, J. Levine, J. Banister, N. Qi; Neutron production and implosion characteristics of a deuterium gas-puff Z pinch. *Phys. Plasmas* 14, 022706 (2007). DOI: https://doi.org/10.1063/1.2446177

[vii] J. E. Bailey; G. A. Chandler; R. C. Mancini; S. A. Slutz; G. A. Rochau; M. Bump; T. J. Buris-Mog; G. Cooper; G. Dunham; I. Golovkin; J. D. Kilkenny; P. W. Lake; R. J. Leeper; R. Lemke; J. J. MacFarlane; T. A. Mehlhorn; T. C. Moore; T. J. Nash; A. Nikroo; D. S. Nielsen; K. L. Peterson; C. L. Ruiz; D. G. Schroen; D. Steinman; W. Varnum, Dynamic hohlraum radiation hydrodynamics, Phys. Plasmas, **13**, No. 5, 056301 (2006). DOI: https://doi.org/10.1063/1.2177640

[viii] G A Rochau, J E Bailey, G A Chandler, G Cooper, G S Dunham, P W Lake, R J Leeper, R W Lemke, T A Mehlhorn, A Nikroo, K J Peterson, C L Ruiz, D G Schroen, S A Slutz, D Steinman, W A Stygar and W Varnum, High performance capsule implosions driven by the Z-pinch dynamic hohlraum, Plasma Phys. Control. Fusion, **49**, B591 (2007). DOI: 10.1088/0741-3335/49/12B/S55

[ix] G. A. Rochau, J. E. Bailey, R. E. Falcon, G. P. Loisel, T. Nagayama, R. C. Mancini, I. Hall, D. E. Winget, M. H. Montgomery, and D. A. Liedahl, "ZAPP: The Z astrophysical plasma properties collaboration," Phys. Plasmas 21, 056308 (2014). DOI: https://doi.org/10.1063/1.4875330

[x] I.R. Lindemuth and R.C. Kirkpatrick, Parameter space for magnetized fuel targets in inertial confinement fusion, Nucl. Fusion 23, 263 (1983). DOI: 10.1088/0029-5515/23/3/001

[xi] Y. B. Khariton, Usp. Fiziol. Nauk 120, 706 (1976) [Sov. Phys. Usp. 19, 1032 (1976)].

[xii] Y C F Thio, Status of the U. S. program in magneto-inertial fusion, J. Phys.: Conf. Ser. 112 042084, (2008).
DOI: 10.1088/1742-6596/112/4/042084

[xiii] S. A. Slutz, M. C. Herrmann, R. A. Vesey, A. B. Sefkow, D. B. Sinars, D. C. Rovang, K. J. Peterson, and M. E. Cuneo, Pulsed-power-driven cylindrical liner implosions of laser preheated fuel magnetized with an axial field, Phys. Plasmas 17, 056303 (2010).
DOI: https://doi.org/10.1063/1.3333505

[xiv] S. A. Slutz and R. A. Vesey, High-Gain Magnetized Inertial Fusion, Phys. Rev. Lett. 108, 025003 (2012).
DOI: https://doi.org/10.1103/PhysRevLett.108.025003

[xv] M. E. Cuneo, M. C. Herrmann, D. B. Sinars, S. A. Slutz, W. A. Stygar, R. A. Vesey, A. B. Sefkow, G. A. Rochau, G. A. Chandler, J. E. Bailey, J. L. Porter, R. D. McBride, D. C. Rovang, M. G. Mazarakis, E. P. Yu, D. C. Lamppa, K. J. Peterson, C. Nakhleh, S. B. Hansen, A. J. Lopez, M. E. Savage, C. A. Jennings, M. R. Martin, R. W. Lemke, B. W. Atherton, I. C. Smith, P. K. Rambo, M. Jones, M. R. Lopez, P. J. Christenson, M. A. Sweeney, B. Jones, L. A. McPherson, E. Harding, M. R. Gomez, P. F. Knapp, T. J. Awe, R. J. Leeper, C. L. Ruiz, G. W. Cooper, K. D. Hahn, J. McKenney, A. C. Owen, G. R. McKee, G. T. Leifeste, D. J. Ampleford, E. M. Waisman, A. Harvey-Thompson, R. J. Kaye, M. H. Hess, S. E. Rosenthal, and M. K. Matzen, Magnetically Driven Implosions for Inertial Confinement Fusion at Sandia National Laboratories, IEEE Trans. Plasma Sci. 40, 3222 (2012).
DOI: 10.1109/TPS.2012.2223488

[xvi] A.B.Sefkow, S.A. Slutz, J.M. Koning, M.M. Marinak, K.J. Peterson, D.B. Sinars, and R.A. Vesey, Design of magnetized liner inertial fusion experiments using the Z facility, Phys. Plasmas **21**, 072711 (2014).
DOI: https://doi.org/10.1063/1.4890298

[xvii] M.R. Gomez, S.A. Slutz, A.B. Sefkow, D.B. Sinars, K.D. Hahn, S.B. Hansen, E.C. Harding, P.F. Knapp, P.F. Schmit, C.A. Jennings, T.J. Awe, M. Geissel, D.C. Rovang, G.A. Chandler, G.W. Cooper, M.E. Cuneo, A.J. Harvey-Thompson, M.C. Herrmann, M.H. Hess, O. Johns, D.C. Lamppa, M.R. Martin, R.D. McBride, K.J. Peterson, J.L. Porter, G.K. Robertson, G.A. Rochau, C.L. Ruiz, M.E. Savage, I.C. Smith, W.A. Stygar, R.A. Vesey, Phys. Rev. Lett. 113, 155003 (2014).
DOI: https://doi.org/10.1103/PhysRevLett.113.155003

[xviii] D. C. Rovang, D. C. Lamppa, M. E. Cuneo, A. C. Owen, J. McKenney, D. W. Johnson, S. Radovich, R. J. Kaye, R. D. McBride, C. S. Alexander, T. J. Awe, S. A. Slutz, A. B. Sefkow, T. A. Haill, P. A. Jones, J. W. Argo, D. G. Dalton, G. K. Robertson, E. M. Waisman, D. B. Sinars, J. Meissner, M. Milhous, D. N. Nguyen, and C. H. Mielke, Pulsed-coil magnet systems for applying uniform 10–30 T fields to centimeter-scale targets on Sandia's Z facility, Rev. Sci. Instrum. **85**, 124701 (2014).
DOI: https://doi.org/10.1063/1.4902566

[xix] M.R. Gomez, S.A. Slutz, A.B. Sefkow, K.D. Hahn, S.B. Hansen, P.F. Knapp, P.F. Schmit, C.L. Ruiz, D.B. Sinars, E.C. Harding, C.A. Jennings, T.J. Awe, M. Geissel, D.C. Rovang, I.C. Smith, G.A. Chandler, G.W. Cooper, M.E. Cuneo, A.J. Harvey-Thompson, M.C. Herrmann, M.H. Hess, D.C. Lamppa, M.R. Martin, R.D. McBride, K.J. Peterson, J.L. Porter, G.A. Rochau, M.E. Savage, D.G. Schroen, W.A. Stygar, R.A. Vesey, Demonstration of thermonuclear conditions in magnetized liner inertial fusion experiments, Phys. Plasmas 22, 056306 (2015).
DOI: https://doi.org/10.1063/1.4919394

[xx]. M.R. Gomez, S.A. Slutz, C.A. Jennings, D.J. Ampleford, M.R. Weis, C.E. Myers, D.A. Yager-Elorriaga, K.D. Hahn, S.B. Hansen, E.C. Harding, A.J. Harvey-Thompson, D.C. Lamppa, M. Mangan, P.F. Knapp, T.J. Awe, G.A. Chandler, G.W. Cooper, J.R. Fein, M. Geissel, M.E. Glinsky, W.E. Lewis, C.L. Ruiz, D.E. Ruiz, M.E. Savage, P.F. Schmit, I.C. Smith, J.D. Styron, J.L. Porter, B. Jones, T.R. Mattsson, K.J. Peterson, G.A. Rochau, D.B. Sinars, Performance Scaling in Magnetized Liner Inertial Fusion Experiments, Phys. Rev. Lett. 125, 155002 (2020).
DOI: https://doi.org/10.1103/PhysRevLett.125.155002

[xxi] P.F. Schmit, P.F. Knapp, S.B. Hansen, M.R. Gomez, K.D. Hahn, D.B. Sinars, K.J. Peterson, S.A. Slutz, A.B. Sefkow, T.J. Awe, E. Harding, C.A. Jennings, G.A. Chandler, G.W. Cooper, M.E. Cuneo, M. Geissel, A.J. Harvey-Thompson, M.C. Herrmann, M.H. Hess, O. Johns, D.C. Lamppa, M.R. Martin, R.D. McBride, J.L. Porter, G.K. Robertson, G.A. Rochau, D.C. Rovang, C.L. Ruiz, M.E. Savage, I.C. Smith, W.A. Stygar, R.A. Vesey, Understanding Fuel Magnetization and Mix Using Secondary Nuclear Reactions in Magneto-Inertial Fusion, Phys. Rev. Lett. 113, 155004 (2014).
DOI: https://doi.org/10.1103/PhysRevLett.113.155004

[xxii] P.F. Knapp, P.F. Schmit, S.B. Hansen, M.R. Gomez, K.D. Hahn, D.B. Sinars, K.J. Peterson, S.A. Slutz, A.B. Sefkow, T.J. Awe, E. Harding, C.A. Jennings, M.P. Desjarlais, G.A. Chandler, G.W. Cooper, M.E. Cuneo, M. Geissel, A.J. Harvey-Thompson, J.L. Porter, G.A. Rochau, D.C. Rovang, C.L. Ruiz, M.E. Savage, I.C. Smith, W.A. Stygar, M.C. Herrmann, Effects of magnetization on fusion product trapping and secondary neutron spectra, Phys. Plasmas 22, 056312 (2015).
DOI: https://doi.org/10.1063/1.4920948

[xxiii] T.J. Awe, R. D. McBride, C. A. Jennings, D. C. Lamppa, M. R. Martin, D. C. Rovang, S. A. Slutz, M. E. Cuneo, A. C. Owen, D. B. Sinars, K. Tomlinson, M. R. Gomez, S. B. Hansen, M. C. Herrmann, J. L. McKenney, C. Nakhleh, G. K. Robertson, G. A. Rochau, M. E. Savage, D. G. Schroen, and W. A. Stygar, Observations of Modified Three-Dimensional Instability Structure for Imploding z-Pinch Liners that are Premagnetized with an Axial Field, Phys. Rev. Lett. **111**, 235005 (2013).
DOI: DOI: https://doi.org/10.1103/PhysRevLett.111.235005

[xxiv] T. J. Awe, C. A. Jennings, R. D. McBride, M. E. Cuneo, D. C. Lamppa, M. R. Martin, D. C. Rovang, D. B. Sinars, S. A. Slutz, A. C. Owen, K. Tomlinson, M. R. Gomez, S. B. Hansen, M. C. Herrmann, M. C. Jones, J. L. McKenney, G. K. Robertson, G. A. Rochau, M. E. Savage, D. G. Schroen, and W. A. Stygar, Modified helix-like instability structure on imploding z-pinch liners that are pre-imposed with a uniform axial magnetic field, Phys. Plasmas **21**, 056303 (2014).
DOI: https://doi.org/10.1063/1.4872331

[xxv] R. D. McBride, S. A. Slutz, C. A. Jennings, D. B. Sinars, M. E. Cuneo, M. C. Herrmann, R. W. Lemke, M. R. Martin, R. A. Vesey, K. J. Peterson, A. B. Sefkow, C. Nakhleh, B. E. Blue, K. Killebrew, D. Schroen, T. J. Rogers, A. Laspe, M. R. Lopez, I. C. Smith, B. W. Atherton, M. Savage, W. A. Stygar, and J. L. Porter, Penetrating Radiography of Imploding and Stagnating Beryllium Liners on the Z Accelerator, Phys. Rev. Lett. 109, 135004 (2012).
DOI: 10.1103/PhysRevLett.109.135004

[xxvi] R. D. McBride, M. R. Martin, R. W. Lemke, J. B. Greenly, C. A. Jennings, D. C. Rovang, D. B. Sinars, M. E. Cuneo, M. C. Herrmann, S. A. Slutz, C. W. Nakhleh, D. D. Ryutov, J.-P. Davis, D. G. Flicker, B. E. Blue, K. Tomlinson, D. Schroen, R. M. Stamm, G. E. Smith, J. K. Moore, T. J. Rogers, G. K. Robertson, R. J. Kamm, I. C. Smith, M. Savage, W. A. Stygar, G. A. Rochau, M. Jones, M. R. Lopez, J. L. Porter, and M. K.

Matzen, Beryllium liner implosion experiments on the Z accelerator in preparation for magnetized liner inertial fusion, Phys. Plasmas **20**, 056309 (2013).
DOI: https://doi.org/10.1063/1.4803079

[xxvii] P. F. Schmit, A. L. Velikovich, R. D. McBride, and G. K. Robertson, Controlling Rayleigh-Taylor Instabilities in Magnetically Driven Solid Metal Shells by Means of a Dynamic Screw Pinch, Phys. Rev. Lett. 117, 205001 (2016).
DOI: https://doi.org/10.1103/PhysRevLett.117.205001

[xxviii] G. A. Shipley, C. A. Jennings, and P. F. Schmit, Design of dynamic screw pinch experiments for magnetized liner inertial fusion, Phys. Plasmas 26, 102702 (2019).
DOI: https://doi.org/10.1063/1.5120529

[xxix] G. A. Shipley, D. E. Ruiz, C. A. Jennings, D. A. Yager-Elorriaga, and P. F. Schmit, Numerical study of implosion instability mitigation in magnetically driven solid liner dynamic screw pinches, Phys. Plasmas 31, 022704 (2024).
DOI: https://doi.org/10.1063/5.0189042

[xxx] V. I. Oreshkin, Thermal instability during an electrical wire explosion, Phys. Plasmas 15, 092103 (2008).
DOI: https://doi.org/10.1063/1.2966121

[xxxi] A. G. Rousskikh, V. I. Oreshkin, S. A. Chaikovsky, N. A. Labetskaya, A. V. Shishlov, I. I. Beilis, and R. B. Baksht, Study of the strata formation during the explosion of a wire in vacuum, Phys. Plasmas 15, 102706 (2008).
DOI: https://doi.org/10.1063/1.3000390

[xxxii] K. J. Peterson, D. B. Sinars, E. P. Yu, M. C. Herrmann, M. E. Cuneo, S. A. Slutz, I. C. Smith, B. W. Atherton, M. D. Knudson, and C. Nakhleh, Electrothermal instability growth in magnetically driven pulsed power liners, Phys. Plasmas 19, 092701 (2012).
DOI: https://doi.org/10.1063/1.4751868

[xxxiii] A. B. Sefkow, "On the helical instability and efficient stagnation pressure production in thermonuclear magnetized inertial fusion," invited talk at 58th Annual Meeting of American Physical Society Division of Plasma Physics [Bull. Am. Phys. Soc. 61(18), UI3.00006 (2016)].
[xxxiv] D. D. Ryutov, T. J. Awe, S. B. Hansen, R. D. McBride, K. J. Peterson, D. B. Sinars, and S. A. Slutz, Effect of axial magnetic flux compression on the helical mode of the magnetic Rayleigh-Taylor instability (theory), AIP Conf. Proc. 1639, 63–66 (2014).
DOI: https://doi.org/10.1063/1.4904778

[xxxv] C. E. Seyler, M. R. Martin, and N. D. Hamlin, Helical instability in MagLIF due to axial flux compression by low-density plasma, Phys. Plasmas 25, 062711 (2018).
DOI: https://doi.org/10.1063/1.5028365

[xxxvi] C. E. Seyler, Axial magnetic flux amplification in Hall-magnetohydrodynamic simulations of externally magnetized z-pinches, Phys. Plasmas 27, 092102 (2020).
DOI: https://doi.org/10.1063/5.0011833

[xxxvii] J.M. Woolstrum, C.E. Seyler, and R.D. McBride, Hall instability driven seeding of helical magneto-Rayleigh–Taylor instabilities in axially premagnetized thin-foil liner Z-pinch implosions, Phys. Plasmas, 29, 122701 (2022).

DOI: https://doi.org/10.1063/5.0103651

[xxxviii] J.M. Woolstrum, D.E. Ruiz, N.D. Hamlin, K. Beckwith, and M.R. Martin, Hall interchange instability as a seed for helical magneto Rayleigh–Taylor instabilities in magnetized liner inertial fusion Z-Pinches scaled from Z-Machine parameters to a next generation pulsed power facility, Phys. Plasmas, 30, 072712 (2023).
DOI: https://doi.org/10.1063/5.0156806

[xxxix] M. R. Weis, P. Zhang, Y. Y. Lau, P. F. Schmit, K. J. Peterson, M. Hess, R. M. Gilgenbach, Coupling of sausage, kink, and magneto-Rayleigh-Taylor instabilities in a cylindrical liner. *Phys. Plasmas*, 22 032706 (2015).
DOI: https://doi.org/10.1063/1.4915520

[xl] L. Atoyan, D. A. Hammer, B. R. Kusse, T. Byvank, A. D. Cahill, J. B. Greenly, S. A. Pikuz, T. A. Shelkovenko, Helical plasma striations in liners in the presence of an external axial magnetic field. *Phys. Plasmas*, 23, 022708 (2016).
DOI: https://doi.org/10.1063/1.4942787

[xli] D. A. Yager-Elorriaga, P. Zhang, A. M. Steiner, N. M. Jordan, P. C. Campbell, Y. Y. Lau, R. M. Gilgenbach, Discrete helical modes in imploding and exploding cylindrical, magnetized liners. *Phys. Plasmas*, 23, 124502 (2016).
DOI: https://doi.org/10.1063/1.4969082

[xlii] D. A. Yager-Elorriaga, P. Zhang, A. M. Steiner, N. M. Jordan, Y. Y. Lau, R. M. Gilgenbach, Seeded and unseeded helical modes in magnetized, non-imploding cylindrical liner-plasmas. *Phys. Plasmas,* 23 101205 (2016).
DOI: https://doi.org/10.1063/1.4965240

[xliii] D. A. Yager-Elorriaga, Y. Y. Lau, P. Zhang, P. C. Campbell, A. M. Steiner, N. M. Jordan, R. D. McBride, R. M. Gilgenbach, Evolution of sausage and helical modes in magnetized thin-foil cylindrical liners driven by a Z-pinch. *Phys. Plasmas*, 25, 056307 (2018).
DOI: https://doi.org/10.1063/1.5017849

[xliv] P. C. Campbell, T. M. Jones, J. M. Woolstrum, N. M. Jordan, P. F. Schmit, J. B. Greenly, W. M. Potter, E. S. Lavine, B. R. Kusse, D. A. Hammer, and R. D. McBride, Stabilization of liner implosions via a dynamic screw pinch, Phys. Rev. Lett. 125, 035001 (2020).
DOI: https://doi.org/10.1103/PhysRevLett.125.035001

[xlv] Paul C. Campbell, T. M. Jones, J. M. Woolstrum, N. M. Jordan, P. F. Schmit, A. L. Velikovich, J. B. Greenly, W. M. Potter, E. S. Lavine, B. R. Kusse, D. A. Hammer, R. D. McBride, Liner implosion experiments driven by a dynamic screw pinch. *Phys. Plasmas*, 28, 082707 (2021).
DOI: https://doi.org/10.1063/5.0044906

[xlvi] T.J. Awe, B.S. Bauer, S. Fuelling, and R.E. Siemon. *Threshold for Thermal Ionization of an Aluminum Surface by Pulsed Megagauss Magnetic Field*. Phys. Rev. Lett. **104**, 035001 (2010).
DOI: https://doi.org/10.1103/PhysRevLett.104.035001

[xlvii] T.J. Awe, B.S. Bauer, S. Fuelling, I.R. Lindemuth, R.E. Siemon. *Experimental investigation of thermal plasma formation from thick aluminum surfaces by pulsed multi-megagauss magnetic field.* Phys. Plasmas **17**, 102507 (2010).

DOI: https://doi.org/10.1063/1.3491335

[xlviii] T.J. Awe, B.S. Bauer, S. Fuelling, and R.E. Siemon. *Mitigation of nonthermal plasma production to measure the pulsed magnetic field threshold for the thermal formation of plasma from thick aluminum surfaces*. Phys. Plasmas **18**, 056304 (2011).
DOI: https://doi.org/10.1063/1.3567485

[xlix] T. J. Awe, E. P. Yu, K. C. Yates, W. G. Yelton, B. S. Bauer, T. M. Hutchinson, S. Fuelling, and B. B. Mckenzie. *On the Evolution from Micrometer-Scale Inhomogeneity to Global Overheated Structure During the Intense Joule Heating of a z-Pinch Rod*. IEEE Trans. Plasma Sci., **45**, 584 (2017).
DOI: 10.1109/TPS.2017.2655450

[l] T. M. Hutchinson, T. J. Awe, B. S. Bauer, K. C. Yates, E. P. Yu, W. G. Yelton, and S. Fuelling. *Experimental observation of the stratified electrothermal instability on aluminum with thickness greater than a skin depth*. Phys. Rev. E **97**, 053208 (2018).
DOI: https://doi.org/10.1103/PhysRevE.97.053208

[li] T. M. Hutchinson, T. J. Awe, B. S. Bauer, B. T. Hutsel, D. A. Yager-Elorriaga, K. C. Yates, A. W. Klemmer, M. W. Hatch, S. E. Kreher, E. P. Yu, and M. Gilmore, On the relative importance of the different initial conditions that seed the electrothermal instability, J. Appl. Phys., 130, 153302 (2021).
DOI: https://doi.org/10.1063/5.0063160

[lii] T. M. Hutchinson, T. J. Awe, B. S. Bauer, D. H. Dolan, J. R. Pillars, B. T. Hutsel, E. P. Yu, A. W. Klemmer, and S. E. Kreher. *Photonic Doppler velocimetry of Ohmically exploded aluminum surfaces*. Phys. Plasmas **27**, 052705 (2020).
DOI: https://doi.org/10.1063/1.5140477

[liii] K. C. Yates, B. S. Bauer, S. Fuelling, T. J. Awe, T. M. Hutchinson, V. V. Ivanov, J. Mei, R. S. Bauer, Significant change in threshold for plasma formation and evolution with small variation in copper alloys driven by a mega-ampere current pulse, *Phys. Plasmas*, 26, 042708 (2019).
DOI: https://doi.org/10.1063/1.5066559
[liv] K. C. Yates, T. J. Awe, B. S. Bauer, T. M. Hutchinson, E. P. Yu, S. Fuelling, D. C. Lamppa, M. R. Weis, Initial surface conditions affecting the formation of plasma on metal conductors driven by a mega-ampere current pulse, *Phys. Plasmas*, 27, 082707 (2020).
DOI: https://doi.org/10.1063/5.0003649

[lv] M.W. Hatch, "Non-uniform Joule heating and plasma formation driven by machined 2D and 3D surface perturbations on dielectric coated and bare aluminum rods," invited talk at 66th Annual Meeting of American Physical Society Division of Plasma Physics [Bull. Am. Phys. Soc., NI03.00003 (2024)].

[lvi] T. J. Awe, E. P. Yu, M. W. Hatch, T. M. Hutchinson, K. Tomlinson, W. D. Tatum, K. C. Yates, B. T. Hutsel, B. S. Bauer, Seeding the explosion of a high-current-density conductor in a controlled manner through the addition of micron-scale surface defects, *Phys. Plasmas*, 28, 072104 (2021).
DOI: https://doi.org/10.1063/5.0053898

[lvii] E. P. Yu, T. J. Awe, K. R. Cochrane, K. C. Yates, T. M. Hutchinson, K. J. Peterson, B. S. Bauer, Use of hydrodynamic theory to estimate electrical current redistribution in metals, *Phys. Plasmas*, 27, 052703 (2020).

DOI: https://doi.org/10.1063/1.5143271

[lviii] E. P. Yu, T. J. Awe, K. R. Cochrane, K.J. Peterson, K. C. Yates, T. M. Hutchinson, M.W. Hatch, B. S. Bauer, K. Tomlinson, and D.B. Sinars, Seeding the electrothermal instability through a three-dimensional, nonlinear perturbation Phys. Rev. Lett., 130, 255101 (2023).
DOI: https://doi.org/10.1103/PhysRevLett.130.255101

[lix] E. P. Yu, T. J. Awe, K. R. Cochrane, K.J. Peterson, K. C. Yates, T. M. Hutchinson, M.W. Hatch, B. S. Bauer, K. Tomlinson, and D.B. Sinars, Three-dimensional feedback processes in current-driven metal Phys. Rev. E, 107, 065209 (2023).
DOI: https://doi.org/10.1103/PhysRevE.107.065209

[lx] D. Ryutov, M. Derzon, and M. Matzen, Rev. Mod. Phys. 72, 167 (2000).
DOI: https://doi.org/10.1103/RevModPhys.72.167

[lxi] Kyle J. Peterson, Edmund P. Yu, Daniel B. Sinars, Michael E. Cuneo, Stephen A. Slutz, Joseph M. Koning, Michael M. Marinak, Charles Nakhleh, Mark C. Herrmann; Simulations of electrothermal instability growth in solid aluminum rods. *Phys. Plasmas* 1 May 2013; 20 (5): 056305. https://doi.org/10.1063/1.4802836

[lxii] K. J. Peterson, T. J. Awe, E. P. Yu, D. B. Sinars, E. S. Field, M. E. Cuneo, M. C. Herrmann, M. Savage, D. Schroen, K. Tomlinson, and C. Nakhleh, Electrothermal Instability Mitigation by Using Thick Dielectric Coatings on Magnetically Imploded Conductors, Phys. Rev. Lett. 112, 135002 (2014).
DOI: https://doi.org/10.1103/PhysRevLett.112.135002

[lxiii] T. J. Awe, K. J. Peterson, E. P. Yu, R. D. McBride, D. B. Sinars, M. R. Gomez, C. A. Jennings, M. R. Martin, S. E. Rosenthal, D. G. Schroen, A. B. Sefkow, S. A. Slutz, K. Tomlinson, and R. A. Vesey. *Experimental demonstration of the stabilizing effect of dielectric coatings on magnetically accelerated imploding metallic liners.* Phys. Rev. Lett. **116**, 065001 (2016).
DOI: DOI: https://doi.org/10.1103/PhysRevLett.116.065001

[lxiv] H. Lamb, Hydrodynamics, 6th ed. (Dover, New York, 1932).

[lxv] L. M. Milne-Thomson, Theoretical Hydrodynamics (Dover, New York, 1968).

[lxvi] A.C. Robinson and C.J. Garasi, Three-dimensional z-pinch wire array modeling with ALEGRA-HEDP, Comput. Phys. Commun. 164, 408 (2004).
DOI: https://doi.org/10.1016/j.cpc.2004.06.054

[lxvii] J.H.J. Niederhaus, S.W. Bova, J.B. Carleton, J.H. Carpenter, K.R. Cochrane, M.M. Crockatt, W. Dong, T.J. Fuller, B.N. Granzow, D.A. Ibanez, S.R. Kennon, C.B. Luchini, R.J. Moral, C.J. O'Brien, M.J. Powell, A.C. Robinson, A.E. Rodriguez, J.J. Sanchez, W.A. Scott, C.M. Siefert, A.K. Stagg, I.K. Tezaur, T.E. Voth, J.R. Wilkes, ALEGRA: Finite element modeling for shock hydrodynamics and Multiphysics, Int J Impact Eng, 180, 104693 (2023).

DOI: https://doi.org/10.1016/j.ijimpeng.2023.104693

[lxviii] T. Sjostrom, S. Crockett, and S. Rudin, Multiphase aluminum equations of state via density functional theory, Phys. Rev. B 94, 144101 (2016).
DOI: https://doi.org/10.1103/PhysRevB.94.144101

[lxix] J. Chakrabarty, Theory of Plasticity (McGraw-Hill Book Company, New York, 1987).

[lxx] D.J. Steinberg, S.G. Cochrane, M.W. Guinan. A constitutive model for metals applicable to high-strain rate. J Appl Phys, 51(3), 1498 (1980).
DOI: https://doi.org/10.1063/1.327799

[lxxi] M. P. Desjarlais, J. D. Kress, and L. A. Collins, Electrical conductivity for warm, dense aluminum plasmas and liquids, Phys. Rev. E 66, 025401(R) (2002).
DOI: https://doi.org/10.1103/PhysRevE.66.025401

[lxxii] J. J. MacFarlane, I. E. Golovkin, P. Wang, P. R. Woodruff, and N. A. Pereyra, SPECT3D – A multi-dimensional collisional-radiative code for generating diagnostic signatures based on hydrodynamics and PIC simulation output, High Energy Density Phys. 3, 181 (2007).
DOI: https://doi.org/10.1016/j.hedp.2007.02.016

[lxxiii] D. J. Ampleford, D. A. Yager-Elorriaga, C. A. Jennings, E. C. Harding, M. R. Gomez, A. J. Harvey-Thompson, T. J. Awe, G. A. Chandler, G. S. Dunham, M. Geissel, K. D. Hahn, S. B. Hansen, P. F. Knapp, D. C. Lamppa, W. E. Lewis, L. Lucero, M. Mangan, R. Paguio, L. Perea, G. A. Robertson, C. L. Ruiz, D. E. Ruiz, P. F. Schmit, S. A. Slutz, G. E. Smith, I. C. Smith, C. S. Speas, T. J. Webb, M. R. Weis, K. Whittemore, E. P. Yu, R. D. McBride, K. J. Peterson, B. M. Jones, G. A. Rochau, D. B. Sinars, Controlling morphology and improving reproducibility of magnetized liner inertial fusion experiments, *Phys. Plasmas*, 31, 022703 (2024).
DOI: https://doi.org/10.1063/5.0169981

[lxxiv] Michael G. Mazarakis, William E. Fowler, K. L. LeChien, Finis W. Long, M. Keith Matzen, D. H. McDaniel, R. G. McKee, C. L. Olson, J. L. Porter, S. T. Rogowski, Kenneth W. Struve, W. A. Stygar, Joe R. Woodworth, Alexander A. Kim, Vadim A. Sinebryukhov, Ronald M. Gilgenbach, M. R. Gomez, D. M. French, Y. Y. Lau, Jacob C. Zier, D. M. VanDevalde, R. A. Sharpe, and K. Ward, High-Current Linear Transformer Driver Development at Sandia National Laboratories, IEEE Trans. Plasma Sci. 38, 4 (2010).
DOI: 10.1109/TPS.2009.2035318

[lxxv] Jens Schwarz, Brian Hutsel, Thomas Awe, Bruno Bauer, Jacob Banasek, Eric Breden, Joe Chen, Michael Cuneo, Katherine Chandler, Karen DeZetter, Mark Gilmore, Matthew Gomez, Hannah Hasson, Maren Hatch, Nathan Hines, Trevor Hutchinson, Deanna Jaramillo, Christine Kalogeras Loney, Ian Kern, Derek Lamppa, Diego Lucero, Larry Lucero, Keith LeChien, Mike Mazarakis, Thomas Mulville, Robert Obregon, John Porter, Pablo Reyes, Alex Sarracino, Daniel Scoglietti, Gabriel Shipley, Trevor Smith, Brian Stoltzfus, William Stygar, Adam Steiner, David Yager-Elorriaga, Kevin Yates, Mykonos: A pulsed power driver for science and innovation, High Energy Density Physics, 53, 101144 (2024).
DOI: https://doi.org/10.1016/j.hedp.2024.101144.

[lxxvi] M. S. Di Capua and D. G. Pellinen, Propagation of power pulses in magnetically insulated vacuum transmission lines, J. Appl. Phys. 50, 3713 (1979).
DOI: https://doi.org/10.1063/1.326277

[lxxvii] J. P. Chittenden, S. V. Lebedev, C. A. Jennings, S. N. Bland, and A. Ciardi, X-ray generation mechanisms in three-dimensional simulations of wire array Z-pinches, Plasma Phys. Controlled Fusion 46, B457 (2004).
DOI 10.1088/0741-3335/46/12B/039

[lxxviii] H.E. Knoepfel, Magnetic Fields (John Wiley & Sons, Inc., New York, 2000).

[lxxix] See https://www.ansys.com/products/electronics/ansys-maxwell for information regarding the Maxwell software package

[lxxx] G. A. Shipley, T. J. Awe, B. T. Hutsel, S. A. Slutz, D. C. Lamppa, J. B. Greenly, and T. M. Hutchinson. *Megagauss-level magnetic field production in cm-scale auto-magnetizing helical liners pulsed to 500 kA in 125 ns.* Phys. Plasmas **25**, 052703 (2018).
DOI: https://doi.org/10.1063/1.5028142

[lxxxi] G. A. Shipley, T. J. Awe, B. T. Hutsel, J. B. Greenly, C. A. Jennings, and S. A. Slutz. *Implosion of auto-mag helical liners on the Z Facility.* Phys. Plasmas **26**, 052705 (2019).
DOI: https://doi.org/10.1063/1.5089468

[lxxxii] See https://andor.oxinst.com/products/istar-intensified-cameras for specifications on Andor iStar Model ICCD cameras.

[lxxxiii] Welch, B. L. (1938). THE SIGNIFICANCE OF THE DIFFERENCE BETWEEN TWO MEANS WHEN THE POPULATION VARIANCES ARE UNEQUAL, *Biometrika*, 29(3-4), 350-362 (1938).
DOI: https://doi.org/10.1093/biomet/29.3-4.350

[lxxxiv] A.C. Robinson, et al. ALEGRA: an arbitrary Lagrangian-Eulerian multimaterial, multiphysics code, in: Proceedings of the 46th AIAA Aerospace Sciences Meeting AIAA-2008-1235, 2008.
DOI: http://dx.doi.org/10.2514/6.2008-1235

[lxxxv] A Loctite 4311 datasheet can be found at https://datasheets.tdx.henkel.com/LOCTITE-4311-en_GL.pdf